Applied Nanoscience (2020) 10:3875–3899
https://doi.org/10.1007/s13204-020-01475-y

ORIGINAL ARTICLE

A comparative study of dirac 2D materials, TMDCs and 2D insulators with regard to their structures and photocatalytic/sonophotocatalytic behavior

A. Raza[1,2] · U. Qumar[2] · J. Hassan[2] · M. Ikram[1] · A. Ul-Hamid[3] · J. Haider[4] · M. Imran[5] · S. Ali[2]

Received: 5 May 2020 / Accepted: 3 June 2020 / Published online: 10 June 2020

Abstract

A new era in the development of advanced functional materials was partly sparked by the discovery of 2D materials. In this respect, graphene is believed to have marked the origin of 2D materials. The ability to fabricate a vast majority of such advanced nanomaterials hinges upon the strength of interplanar interactions realized in their respective bulk counterparts. The present study undertakes the comparative analysis of oft-explored 2D materials such as Dirac 2D materials (GO, rGO), TMDCs (MoS_2) and 2D insulators (BN) in the context of their structural, optical, thermal and morphological parameters. Despite implementing several methodologies including a combination of physical, chemical and biological techniques, aquatic and microbial pollution remains a challenge to this day. More recently, nanomaterials have attracted considerable attention as these are believed to hold an extraordinary prospective for utilization toward environmental remediation. Among several probable candidates, 2D materials hold immense appeal due to its useful properties including high absorptivity and large surface area, which enable them to be employed for multifaceted applications. In the present study, a wide range of experimental results extracted from numerous characterization techniques (i.e., XRD, UV–Vis, FTIR, HR-TEM, XPS, DSC-TGA, and Raman) is included. For instance, optical data obtained from these materials point toward a narrow bandgap, while HR-TEM images show large surface area, which suggests that these materials hold promising prospect for use in applications that require strong catalytic activity. Further experimental results indicate that photocatalytic and sonophotocatalytic potential is significantly enhanced by 2D materials. In this respect, rGO showed 60% degradation of synthetic pollutant in 100 min and MoS_2 realized 55% degradation during the same duration. The present study suggests that rGO may be used as a superior photocatalyst in wastewater treatment and related environmental applications. Moreover, the sonophotocatalytic behavior exhibited by these materials showed consistently higher efficiency compared to the respective individual processes which is attributed to the formation of larger amounts of electron–hole pairs.

Keywords TMDCs · Nanosheets · Nanopetals · Photocatalyst · Sonophotocatalyst · XPS · DSC-TGA

✉ M. Ikram
dr.muhammadikram@gcu.edu.pk

[1] Solar Cell Applications Research Lab, Department of Physics, Government College University Lahore, Punjab 54000, Pakistan

[2] Department of Physics, Riphah Institute of Computing and Applied Sciences (RICAS), Riphah International University, 14 Ali Road, Lahore, Pakistan

[3] Center for Engineering Research, Research Institute, King Fahd University of Petroleum & Minerals, Dhahran 31261, Saudi Arabia

[4] Tianjin Institute of Industrial Biotechnology, Chinese Academy of Sciences, Tianjin 300308, China

[5] State key Laboratory of Chemical Resource Engineering Beijing Advanced Innovation Centre for Soft Matter Science and Engineering, Beijing Engineering Center for Hierarchical Catalysts, Beijing University of Chemical Technology, Beijing 100029, China

Introduction

Research in two-dimensional (2D) materials exploded on the heels of isolation of graphene in 2004. Graphene formed the basis for the development of advanced 2D materials (Beshkova and Yakimova 2020; Chenet 2016). These materials, also referred to as 2D topological or single-layered materials, have a thickness of a few nanometers and exhibit a range of exceptional properties (Vargas-Bernal 2016). Single-layered materials possess ultra-low weight, high strength, large Young's modulus, superior charge carrier mobility, high conductivity and long spin diffusion length, which are suitable for use in spintronics devices. Moreover, anisotropy between in-plane and out-plane results in improved mechanical properties (Li et al. 2017; Geng and Yi 2019). The adjacent atoms in a plane are linked through covalent bonding, whereas stacking of layers provides stability due to van der Waals (vdW) interactions (Li et al. 2017). Furthermore, a newly developed material system using graphene-coated surface has been shown to realize macroscale lubricity on macroscale surfaces under ambient conditions (Zhang et al. 2020a), which up until recently was considered not feasible. In addition, due to large specific surface area, high electrical conductivity and good stability, graphene and its derivatives such as graphene oxide (GO) and reduced graphene oxide (rGO) have been employed as catalyst supports resulting in enhanced electrocatalytic activity and durability. To cite an example, rGO-supported PtPd nanocubes possess outstanding electrocatalytic activity toward methanol oxidation reaction in an acidic electrolyte, as compared to unsupported PtPd nanocubes and commercial Pt/carbon black (Liu et al. 2019a; Zhang et al. 2020b). Furthermore, nanomaterials are widely employed to develop novel environment-friendly slurries and technologies. This paves the way to fabricate high performance devices for use in aerospace, semiconductor and microelectronics industries, which is extremely difficult to manufacture with conventional technologies. More importantly, research in nanomaterials contributes toward eliminating pollution induced by traditional manufacturing and industries (Zhang et al. 2017a, 2018, 2019). On the other hand, a tremendous increase in the production and usage of graphene-based nanomaterials for biomedical purposes raises concerns about their effects on humans and environment. It is, therefore, necessary to understand the interaction of these nanomaterials with life forms to advance the biomedical application of nanomaterials. Although, the health effects associated with graphene-based nanomaterials have been studied at the cellular level and in animal models, the consequences of human exposure are vastly unknown. It has been shown that humans can be affected by graphene-based nanomaterials via several exposure routes (Zhang et al. 2012; Wang et al. 2018a; Cui et al. 2019; Rashid 2020).

Herein, it is crucial to explore reliable routes to synthesize 2D materials. Several approaches such as micromechanical exfoliation, ultrasonic chemical exfoliation, plasma cracking of hydrocarbons, chemical vapor deposition (CVD), hydrothermal technique, and topochemical transformation have been employed to synthesize single-layered materials (Wang et al. 2016; Tun and Naing 2020). Among these methods, top-down exfoliation (chemical exfoliation) and hydrothermal technique present numerous advantages including low cost, solution processibility, and ability to maintain sustainable output. These techniques have shown excellent potential for use in various vital areas. A variety of morphologies such as nanopetals, flowers, nanowires, and nanorods have been synthesized with these techniques. Therefore, in the current study, these two approaches are used to synthesize nanosheets and nanopetals (Cai et al. 2018; Feng and Li 2017).

The 2D materials can be categorized as Dirac 2D materials, transition metal dichalcogenides (TMDCs), 2D insulators, mono-element 2D materials, and an emerging class known as MXenes (Beshkova and Yakimova 2020). In the present article, the first three categories listed above are discussed. The first category includes Dirac 2D materials that exhibit Dirac cone-like band structure typology. It consists of semi-metals with valence band (VB) and conduction bands (CB) about their Brillouin point formed as inversed cones that touch at their vertex, and possess "massless" fermions around that point. This permits the production of auspicious electrons that are unique and distinguished from standard electrons emitted by metals (Feng and Li 2017; Ng 2019). Graphene, because of its favorable energy state of sp^2 hybridization, is the most stable Dirac material. Graphene is referred to as semi-metal owing to its π–π^* band structure. In graphene, VB and CB are symmetrical around Dirac point, thus electronic properties are defined close to K point in the Dirac equation and not by Schrödinger equation (Beshkova and Yakimova 2020; Hasan et al. 2020; Li et al. 2018; Manzeli et al. 2017; Li and Zhu 2015). In addition, graphene oxide (GO) which is an oxidized form of graphene preserves all properties of graphene (Beshkova and Yakimova 2020; Hasan et al. 2020; Li et al. 2018). Apart from graphene, allotropes of Si and Ge, i.e., silicene and germanene, respectively, also belong to Dirac 2D materials, which are unstable and exclusively synthetic (Beshkova and Yakimova 2020; Manzeli et al. 2017).

The next emerging and eye-catching class of 2D materials are TMDCs that show semiconductor behavior of the type MX_2, where M is known as a transition metal and X is a chalcogen. It consists of a monolayer of M (W, Mo, Zr, Nb, Ta, Ti, and Hf, etc.) sandwiched between two X

(S, Se, Te) atoms. These materials possess remarkable catalytic, photoluminescence, direct bandgap, and water resistance properties and also show higher structural rigidity as compared to graphene or boron nitride. There are approximately 60 TMDCs identified so far. Among these, MoS_2 has gained much attention due to its ability to show 2H phase (semiconductor), 1T (metallic nature) and 3R (standard and stable condition) polytypes (Hasan et al. 2020; Li et al. 2018; Manzeli et al. 2017). In monolayer configuration, it exhibits 1.8 eV direct bandgap. This property enables it to compensate for the shortcoming in gapless graphene and consequently opens doors for its use in switching and optoelectronic systems as well as catalytic applications in the future (Li and Zhu 2015).

The third class of widely researched 2D insulators is boron nitride (BN), which is isostructural to graphene. It has an equal concentration of boron and nitrogen atoms and shows exotic properties similar to graphite. Monolayer BN, which can be extracted as a stable material from its bulk form, exhibits a bandgap of 5.9 eV. Moreover, in crystalline form, BN occurs in three key structural configurations; hexagonal BN (h-BN) that resembles graphite, sphalerite BN (β-BN) comparable to cubic diamond, and lastly wurtzite BN (ɣ-BN) that is structurally analogous to diamond (Beshkova and Yakimova 2020; Zhang et al. 2017b; Yuan et al. 2016). The h-BN exhibits valuable optoelectronic properties. It is mechanically robust, chemically inert, and possesses high thermal stability. Although it behaves as an insulator, its properties and functionality can be modified systematically using various strategies such as doping, hybridization, and substitution making it a promising functional material that is highly suitable for numerous applications (Beshkova and Yakimova 2020; Zhang et al. 2017b).

The aforementioned 2D materials have contributed to several key developments in advanced materials research. It has fulfilled wafer-scale growth requirements for numerous materials that have eventually led to several industrial applications in areas including sensors, solar cells, biotechnology, transportation, energy, and environmental sectors. (Morgan et al. 2019). A clean environment is one of the most challenging issues faced by humankind today. In recent decades, inadequate access to drinking water has become a global concern. Rapid population growth and industrialization have contributed to the rising environmental pollution, with approximately 750 million people estimated to live without proper access to sufficiently clean water (Raza et al. 2019; Rafiq et al. 2019; Junaid et al. 2019). Various techniques including ion exchange, electrolysis, carbon filter, chemical coagulation, biological procedures, membrane filtration and reverse osmosis (RO) have been employed to address the problem of water pollution. However, these methods are marred by inefficiency, complicated processes, high sludge composition, high capital and operational costs, and high energy usage (Raza et al. 2019; Ikram et al. 2020a; Sattar et al. 2019). Therefore, researches into the development of enhanced technologies for water treatment continue. One such technique is photocatalysis which overcomes most of the deficiencies mentioned above. Photocatalytic potential of inorganic semiconductor nanomaterials has attracted researchers due to its admirable physical and chemical properties such as low toxicity, electrochemical stability, excellent oxidant performance, cost-effectiveness and environmental viability (Altaf 2020; Khurshid et al. 2019). Research in water treatment has shown that graphitic carbon allows transport of photoelectron and greatly improves photo-efficiency of the system due to a large number of delocalized electrons conjugated to sp^2 carbon network. The GO nanosheets demonstrate a high absorption rate of organic materials in an aqueous solution. Hence, GO and rGO permit photocatalysis reaction and can be considered as visible light active photocatalysts (Kumar et al. 2019; Dadvar et al. 2017). Transition metal dichalcogenide material such as MoS_2 leads to suitable changes in redox potential that permit it to act as visible light-reactive photocatalyst. Moreover, conduction and valence band electronic states predominantly originate from Mo 4d orbitals. This suggests that photo-excited electron does not considerably weaken bonds between Mo and S atoms, which allows for boosted photochemical stability. The visible light response of photocatalysts based on TMDCs nanostructures finds a variety of applications in contrast with other traditional photocatalysts, such as ZnO and TiO_2 possessing large bandgap (> 3 eV) which may only react under UV irradiations (Mishra et al. 2015).

Catalytic behavior and antimicrobial potential of these materials have been studied by the same team of authors previously (Raza et al. 2019; Ikram et al. 2020a, b, c, e, f, g; Qumar et al. 2020; Hassan et al. 2020; Aqeel et al. 2019). In the present work, 2D materials were synthesized and a comparative study was undertaken to evaluate their structural, optical, chemical, and photocatalytic properties in the presence and absence of an ultrasonic bath. Two experiments including photocatalytic and sonophotocatalytic activity were performed for evaluation of catalytic behavior.

Experimental section

Materials

Graphite (99%), sulfuric acid (H_2SO_4, 37%), sodium nitrate ($NaNO_3$, 99.9%,) and phosphoric acid (H_3PO_4) were procured from Sigma-Aldrich. Potassium permanganate ($KMnO_4$, 99%) and hydrochloric acid (HCl) were acquired from Merck. For the synthesis of MoS_2 nanopetals, sodium molybdate dehydrate ($Na_2MoO_4{\cdot}2H_2O$, 99%), thiourea

(NH_2CSNH_2, 99%) and oxalic acid ($H_2C_2O_4$) were purchased from Sigma-Aldrich. For the preparation of boron nitride nanosheets, bulk boron nitride, dimethylformamide (DMF) and ethanol were attained from Sigma-Aldrich.

Synthesis of graphene oxide (GO)

Graphene oxide was synthesized by adopting a modified Hummers method. Firstly, in this process, graphite powder (5 g) was mixed with sodium nitrate-$NaNO_3$ (2.5 g) in the presence of sulfuric acid-H_2SO_4 (108 ml) and 12 ml phosphoric acid. The mixture was magnetically blended and moved to an ultrasonic bath for 10 min. After filtration, the solution was dried for about 2 h in a muffle furnace at 60 °C, until complete elimination of moisture occurred. $KMnO_4$ (15 g) was incorporated slowly to the above mixture at ~ 5 °C. Subsequently, suspension was transferred to the ice bath and stirred for 2 h. The suspension temperature was held at 98 °C for 1 h, while deionized water (DIW) was continuously added up to 400 ml of suspension volume. After 5 min, H_2O_2 (15 ml) was added. Subsequently, the acquired product was centrifuged and washed thoroughly with DIW and 5% HCl and later dried at 60 °C. Upon synthesis, the pH of GO was measured at 5.7, as shown in Fig. 1 (Song et al. 2014; Alam et al. 2017). Reduced form of GO (rGO) was obtained from synthesized GO using thermal reduction at a temperature of 300 °C. This was undertaken by increasing the temperature rapidly, which serves to remove the oxygen atoms and attached functional groups from carbon planes leading to exfoliation of GO to produce rGO, as shown in Fig. 1 (Sengupta et al. 2018). The rGO may be considered as chemically derived GO that exhibits diversity in structure from single layer to multilayers (Le et al. 2018).

Synthesis of MoS_2 nanopetals

The hydrothermal route was adopted for the synthesis of pristine MoS_2 nanopetals, as shown in Fig. 2, In brief, thiourea (1.4 g) and sodium molybdate dehydrate (1 g) were dissolved vigorously in deionized water (80 ml) in an ultrasonic bath for 10 min. Herein, $Na_2MoO_4{\cdot}2H_2O$ donates Mo to the process, while NH_2CSNH_2 was used as a source of S. The preparation proceeds by the addition of 0.4 g of oxalic acid to maintain pH value of the solution in an acidic regime. The suspension was ultrasonicated again for 20 min, moved to autoclave and sealed tightly. Afterwards, autoclave was shifted into a vacuum oven operated at 170 °C for 20 h. Upon completion of the reaction, the autoclave was cool naturally to room temperature. Acquired blackened product was washed thoroughly with ethanol and DI water several times using ultrasonic cleaning to eliminate impurities and subsequently dried at 50 °C for 5 h (Kumar et al. 2017).

Preparation of h-boron nitride nanosheets

BN nanosheets were extracted from bulk BN through chemical exfoliation. In this regard, bulk BN powder (200 mg) was liquefied in 50 ml of DMF and stirred vigorously for 20 min.

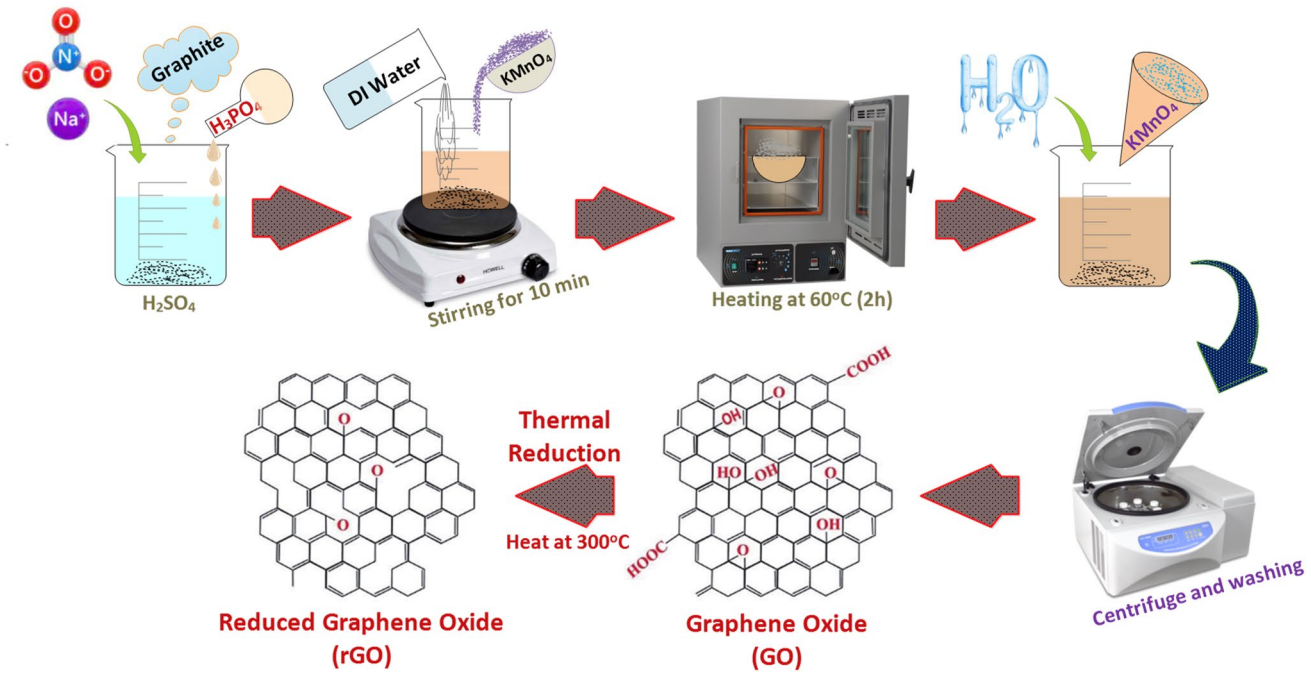

Fig. 1 Illustration showing synthesis of GO and thermal reduction of rGO

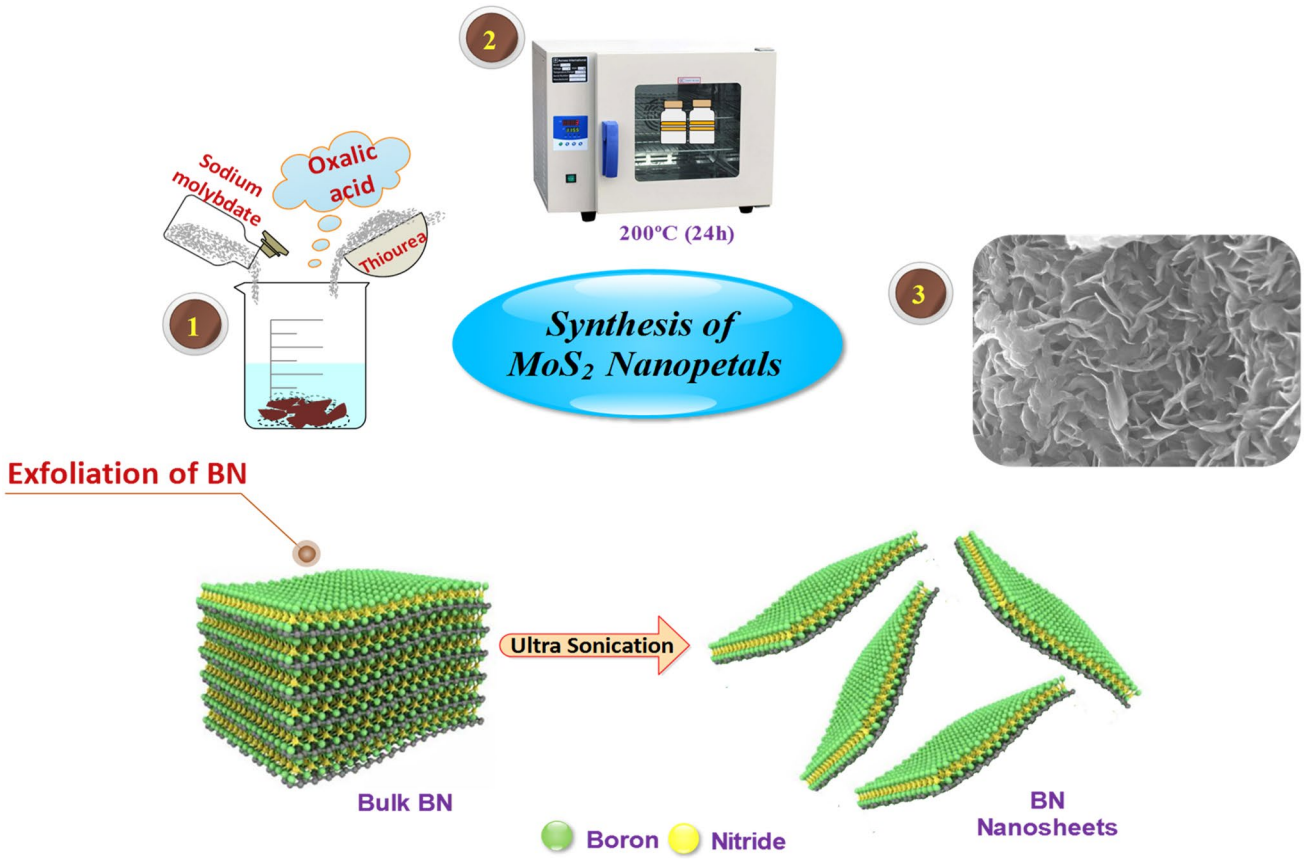

Fig. 2 Various steps involved in the synthesis of MoS_2 nanopetals and exfoliation of bulk BN

Later, solution was transferred to an ultrasonic bath for 12 h at 50 °C. Acquired suspension was centrifuged at 3500 rpm (20 min). Supernant was poured to extract a concentrated solution of exfoliated h-boron nitride nanosheets. The precursor was washed thoroughly with ethanol and DI water to eliminate by-products. Finally, the solution was dehydrated at 100 °C for 6–7 h in a vacuum oven and h-BN nanosheets were collected in powder form. The procedure of above-mentioned experiment is illustrated in Fig. 2 (Zhang et al. 2017c).

Photocatalytic and sonophotocatalytic activity

Photocatalytic activity (PCA) of synthesized materials using sunlight and ultrasonic bath with sunlight (sonophotocatalysis) was assessed by determining the degradation rate of an industrial pollutant namely methylene blue (MB), as illustrated in Fig. 3. In this regard, 5 mg of dye was mixed in 500 ml DIW under vigorous stirring. 10 mg suspension of photocatalyst (GO, rGO, MoS_2, BN) was mixed with prepared solution and placed in dark for at least 30 min to enable substantial absorbance. Later, 60 ml of solution for each photocatalyst was taken and ultrasonicated for 20 min. Afterwards, the solution was transferred to a photoreactor operated with mercury lamp (400 W with 400–700 nm) as a visible light source (sun). The distance between the light source and solution was maintained at 15 cm to prevent excessive heating. The degree of sonophotocatalytic degradation undertaken by catalysts was determined using rectangular shaped ultrasonic bath (XUB6; Grant Co., Ltd., England) operated at a fixed frequency of 35 kHz and an ultrasonic power of 200 W. The same beaker was placed in the center of ultrasonic bath under visible light source. After exposure to light for 20 min, 3 ml solution was withdrawn to measure dye reduction capability. The absorption spectrum of MB was examined through UV–Vis spectrophotometer. The same procedure was followed for all samples and the degradation efficiency was calculated as follows:

$$\text{Degradation efficiency } (\%) = \left(\frac{C_o - C}{C_o}\right) \times 100.$$

In the above equation, C_o corresponds to initial absorbance (i.e., $t = 0$) and C refers to the final absorbance at time t (Rafiq et al. 2019; Suresh et al. 2018). Collected solution was centrifuged at 4000 rpm for 5 min to remove photocatalyst

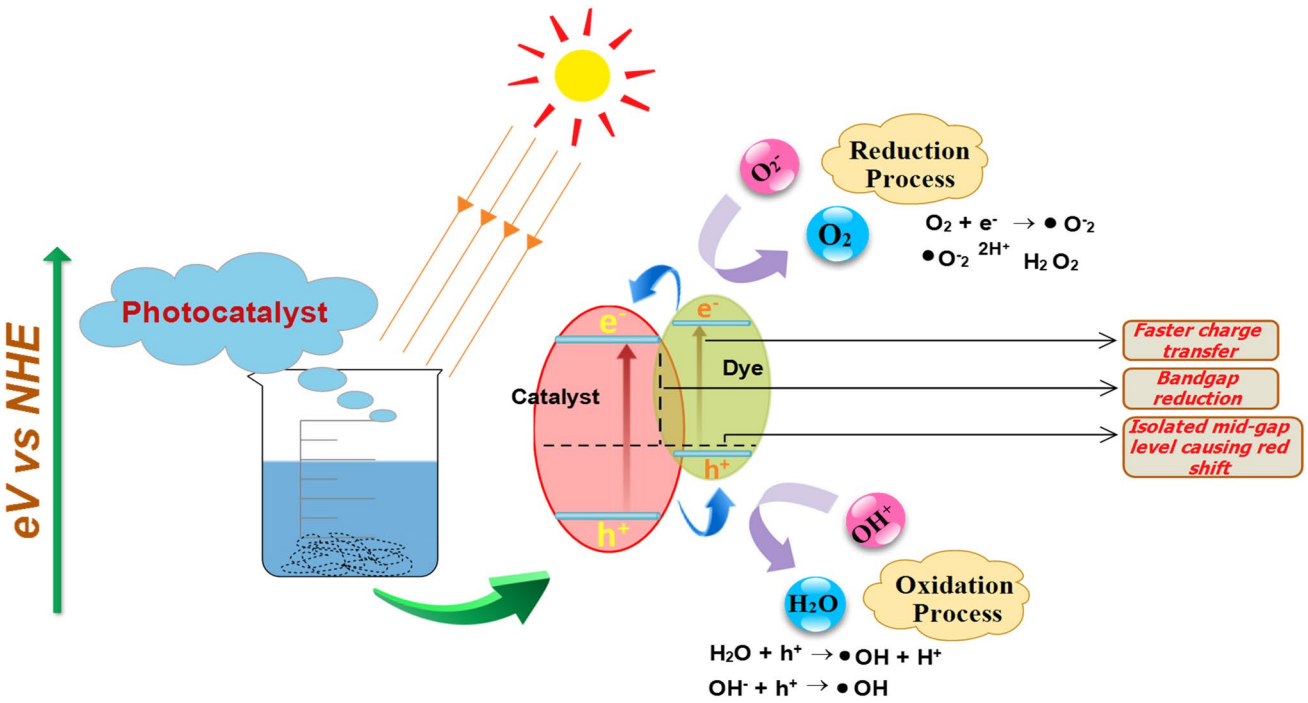

Fig. 3 Photocatalytic and Sonophotocatalytic mechanism for dye degradation in the presence of photocatalyst

from the solution; similar procedure was undertaken for SPCA.

Reaction mechanism

The photocatalysis principle is shown schematically in Fig. 3, where electronic band structures of semiconducting materials are visible. An electron (e^-) in the valence band-VB is excited by photo-radiation to an unoccupied conduction band-CB, which are separated by forbidden bandgap, leaving a positive hole (h^+) in VB. The formation of excitons (e^- –h^+ pair) initiates oxidation and reduction reaction within synthetic compounds, which are then absorbed by the surface of photocatalyst. The limitation mentioned above does not hold for electronic band structure of photocatalysts. As an example, isolated chemical species that do not possess aforesaid band structure in solid form may be considered photocatalysts. Even with the use of a bulk material, photo-absorption and the resulting reaction may proceed on localized sites of photocatalyst (Ohtani 2010).

Numerous steps are involved in the transfer of reactants to the surface of photocatalyst:

1. Adsorption of reactants
2. Absorption of visible light photons by catalysts
3. Formation of electron (e^-)-hole (h^+) pairs
4. Migration of e^--h^+ to the surface-active sites of photocatalyst
5. Reaction between adsorbed products and adsorbed reactant species
6. Desorption of products
7. Removal of products from catalyst surface region

The above-mentioned seven steps may be categorized into three main areas namely electronic reactions, surface chemical reactions, and mass transfer (Liu and Li 2014).

Reaction kinetics

A photo-excited electron and positive hole generate a redox reaction that governs the kinetics of a chemical reaction. Thereby, rate constant of these active species can be evaluated. Kinetics of electron–hole recombination depends upon its approach. For excitation as well as recombination of excitons, the rate of combination follows 1st order rate equation, i.e., $-\frac{dA}{dt} = k(A)$, whereas if multiple e^--h^+ originate simultaneously within photocatalyst particle, the rate obeys 2nd order rate equation, i.e., $-\frac{dA}{dt} = k(A)^2$. The overall reaction rate also depends upon recombination ability by considering that k-redox and k-recombination are reaction rate constants corresponding to "e^-" and "h^+" and their recombination. However, no method exists to calculate k (recombination), because recombination does not produce any chemical species (Ohtani 2010). The photocatalyst is irradiated by photons of energy equal/greater than the corresponding bandgap of the photocatalyst:

$$\text{Photocatalyst} + hv \rightarrow e^{-}(CB) + h^{+}(VB). \quad (1)$$

Produced electrons through photons may freely be absorbed by O_2 to generate superoxide radical as $O_2^{\cdot -}$:

$$e^{-} + O_2 \rightarrow O_2^{\cdot -}. \quad (2)$$

Therefore, $O_2^{\cdot -}$ reacts with H_2O to create hydroperoxy radicals-$H_2O^{\cdot}$ and hydroxyl radical-$OH^{\cdot}$, which are strong oxidizing agents that decompose organic pollutants:

$$O_2^{\cdot -} + H_2O \rightarrow HO_2^{\cdot} + OH. \quad (3)$$

Simultaneously, photogenerated holes could be trapped by hydroxyl groups, i.e., H_2O on the surface of a photocatalyst to generate hydroxyl radicals ($OH^{\bullet}$):

$$h^{+} + OH^{-} \rightarrow {}^{\cdot}OH_{ad} \quad (4)$$

$$h^{+} + H_2O \rightarrow {}^{\cdot}OH + H^{+}. \quad (5)$$

Ultimately, organic molecules are oxidized to produce CO_2 and H_2O as follows:

$$OH + \text{organic molecules} + O_2 \rightarrow \text{products}\left(CO_2 \text{and } H_2O\right). \quad (6)$$

Temporarily, slight recombination of e^{-}-h^{+} might take place which could reduce photocatalytic activity of prepared nanocatalyst (Gnanaprakasam et al. 2015):

$$e_{CB}^{-} + h_{VB}^{+} \rightarrow \text{Photocatalyst}. \quad (7)$$

Materials characterization

Crystal structure and phase purity of samples were evaluated with XRD using Spectrum Bruker system (X-ray diffraction (XRD), D2 Phaser, USA) equipped with Cu Kα radiation. Chemical analysis and study of attached functional groups were undertaken using FTIR Perklin Elmer 3100 spectrometer. Optical properties were analyzed through UV–Vis Spectrophotometer (Genesys 10S) ranging from 200 to 700 nm. Surface morphology and d-spacing of synthesized specimens were observed through FESEM along with EDS spectrometer, JSM-6460LV, and HR-TEM (Philips CM30 and JEOL JEM 2100F). Raman microscope with a $\lambda = 532$ nm (6 mW) laser was employed to explore molecular vibrational mode as well as to record structural fingerprint. Photoluminescence-PL spectroscopy was carried out to probe migration and recombination of electron–hole pairs using a spectrofluorometer (JASCO, FP-8300). Thermal behavior and weight loss were measured using TGA, SDT Q600 (TA Instrument) in a controlled environment, at 1000 °C with 10 °C min^{-1} ramp rate. XPS was undertaken with Thermo-VG Scientific ESCALAB 250 equipped with a monochromatic Al Kα x-ray source.

Results and discussion

In case of MoS_2, observed peaks located around ~ 14.2°, 33.5°, 38.5°, 44°, 58° and 70° are indexed as (002), (101), (103), (006), (110) and (108) planes, respectively. The data confirms the presence of hexagonal structure of MoS_2 (2H-MoS_2) which is consistent with JCPDS 00-37-1492 of $P6_3/mmc$ space group with lattice constants $a = 3.161$ Å and $c = 12.299$ Å, as shown in Fig. 4a. Within the limits of instrument's sensitivity, no impurity phases are found, which indicates the formation of pure 2H-MoS_2 (Yi and Zhang 2018; Wang and Li 2007; Ma et al. 2016; Veeramalai et al. 2016). In a pattern of MoS_2, two characteristics peaks are detected referred to as (002) and (101). The (002) plane is the basal plane along C axis direction of molecular lamellae of MoS_2 that signifies well-developed layered structure with the enhanced planar crystal structure. It has an interlayer spacing of 0.62 nm that agrees well with HR-TEM observations (see Fig. 7c') (Wang and Li 2007; Ma et al. 2016; Veeramalai et al. 2016). SAED rings of MoS_2 unveil discrete ring features analogous to different planes of 2H-MoS_2 as depicted in Fig. 4. This confirms the formation of a highly crystallized sample that indicates good agreement between XRD and SAED patterns.

XRD profiles of BN show diffraction peaks centered at ~ 26.71°, 41.52°, 43.49° and 50.27°. Observed diffraction profiles agree with crystallographic planes of (002), (100), (101) and (102), respectively, and harmonize well with standard spectrum (JCPDS reference # 00-034-0421). It suggests the presence of hexagonal phase of BN with lattice parameters of $a = b = 2.5044$ Å and $c = 6.6562$ Å including space group $P6_3/mmc$, as shown in Fig. 4a (Ikram et al. 2020e; Tang et al. 2019; Fan et al. 2016b). Interlayer spacing of characteristic peak (d_{002}) at 26.7° evaluated through Bragg's law is 0.34 nm, which corresponds well with the measurement obtained from the HR-TEM image (Fig. 7d'). The value of d-spacing can be considered to be a good indicator of adsorption properties and molecular transport behavior of BN (Tang et al. 2019). In addition, sharpness and intensity of peaks suggest formation of thin layers of BN and weak stacking of nanosheets in preferred c-direction (Zhang et al. 2017c). Indexed SAED ring is consistent with the XRD data obtained from BN nanosheets, as illustrated in Fig. 4. XRD profiles of all samples show good agreement with structural properties that may affect their application.

FTIR was employed to examine attached functional groups and molecular fingerprints with various vibrational bonding modes, ranging from 4000 to 500 cm^{-1}. In IR spectra of GO and rGO, detected peaks are located around

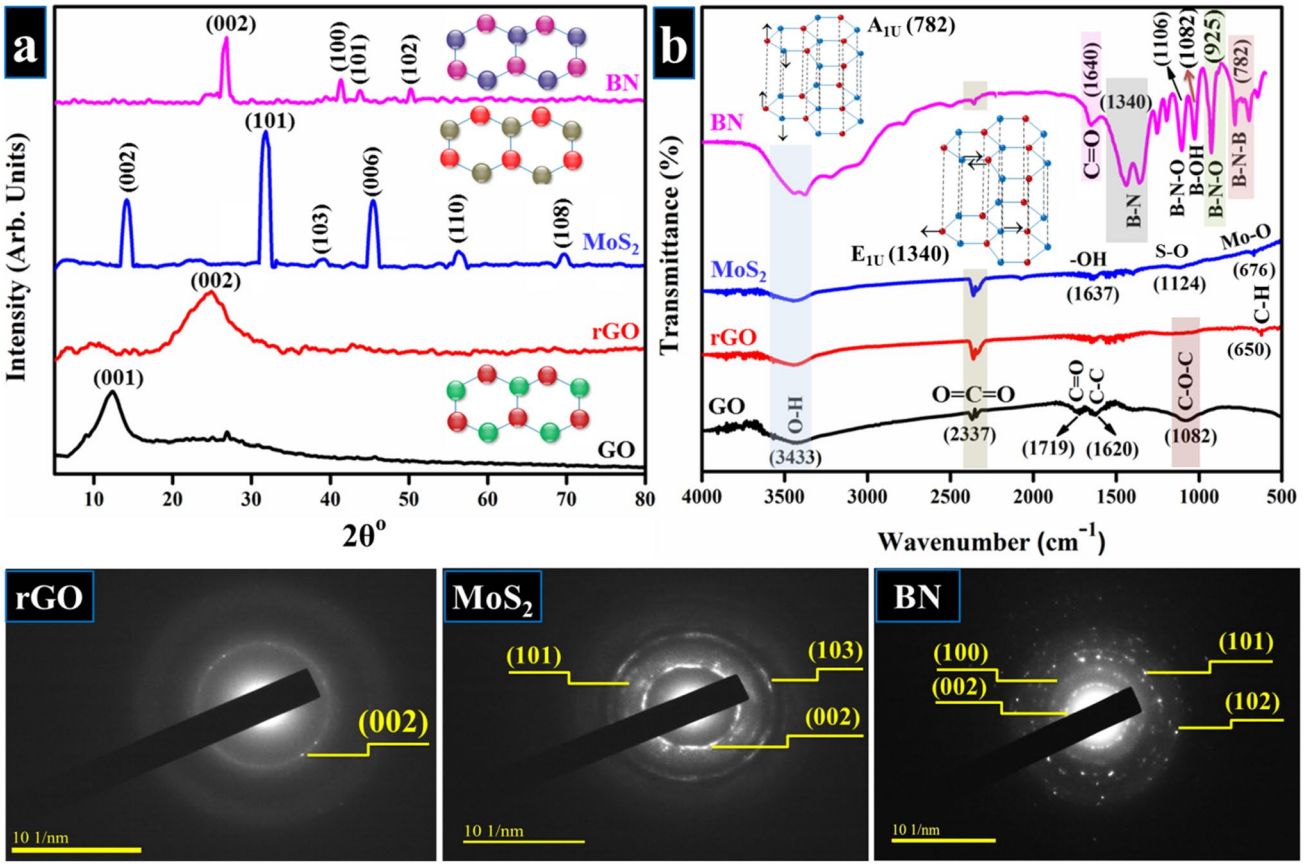

Fig. 4 **a** XRD profiles of prepared samples, **b** FTIR spectra; and corresponding SAED images

1082, 1620, 1719, 2337, 3433 cm^{-1}, as shown in Fig. 4b. The absorption peak at 650 cm^{-1} is an identification region of sp^2 configured carbon bonding assigned to C–H bending vibration (Ngidi et al. 2019). The low absorption peak at 1082 cm^{-1} is attributed to C–O–C bond formation due to stretching vibrations of hydroxyl groups. Observed peak at 1620 cm^{-1} is designated to aromatic C–C stretching, which is also evident in UV–Vis. data (Aqeel et al. 2019; Some et al. 2013; Luceño-Sánchez et al. 2018; Gurunathan et al. 2015). Peaks observed at 1719 and 2371 cm^{-1} are assigned to C=O stretching vibrations that originate from COOH groups and CO_2, respectively (Aqeel et al. 2019; Church et al. 2016; Eigler et al. 2012). Broad band around 3433 cm^{-1} appeared due to O–H stretching vibration (Aqeel et al. 2019; Some et al. 2013; Gurunathan et al. 2015).

In case of MoS_2, clear transmitted peaks are situated at ~ 676, 1124, 1636, 2337, 3438 cm^{-1}, and assigned to desired functional groups, as demonstrated in Fig. 4b. Two distinctive peaks are found at 676 and 1124 cm^{-1}, which are assigned to Mo–O bonding group and S=O functional group (Fosso-Kankeu et al. 2018). Transmittance detected around 1636 and 3438 cm^{-1} are allocated to hydroxyl (–OH) group and the formation of O–H. Both transmittances correspond to stretching vibrations (Fosso-Kankeu et al. 2018; Vattikuti and Byon 2015; Wang et al. 2016a). The sharp peak observed at 2337 cm^{-1} in all samples is due to intercalation of CO_2 between nanosheets (Church et al. 2016; Eigler et al. 2012; Wang et al. 2018b).

Crystal symmetry of BN is influenced by the vibrational mode of respective bonding, while optical activity under various excitation sources is assessed by selection rules. Optical phonon modes that belong to h-BN at the above-mentioned space group and K point of corresponding Brillouin zone are assumed by Eq. 8 (Geick et al. 1966).

$$K = 2B_{1g} + A_{2u} + E_{1u} + 2E_{2g} \quad (8)$$

In the above equation, $2B_{1g}$ is evaluated optically, which is inactive so it does not appear in the vibrational spectrum. Besides, characteristic E_{1u} and A_{2u} mode are infrared active phonon modes that are attributed to stretching (in-plane) as well as bending (out-of-plane) transverse optical (TO) vibrations, respectively. Former mode identified at 1340 cm^{-1} is referred to B–N, whereas later peak observed at 782 cm^{-1} is ascribed to B–N–B vibrations (Vu et al. 2018; Ding et al. 2018a). The other two peaks situated at ~ 925 and ~ 1106 cm^{-1}

correspond to boron oxy-nitride N–B–O band (stretching vibration) (Kumar et al. 2016). Another peak traced at 1640 cm^{-1} is associated with C=O, while peak centered at 1082 cm^{-1} relates to hydronium ion (–OH). An extensive band observed around 3433 cm^{-1} relates to O–H indicating the presence of moisture, as seen clearly in Fig. 4b (Li et al. 2013).

Optical properties of prepared 2D materials in terms of absorbance of ultra-visible light and bandgap measurement were evaluated with UV–Vis spectrograph (200–700 nm), as displayed in Fig. 5a. In case of Dirac 2D material (GO), spectrum shows characteristic peak at ~ 230 nm that is attributed to π–π* transition in aromatic C–C bonding, which reveals restoring of an extensive conjugated framework of sp^2 carbon atoms. An additional shoulder peak sited around 300 nm is caused by n–π* transitions of C=O bonds (Kumar et al. 2019; Gurunathan et al. 2015; Fan et al. 2016b). Comparatively, in the study of rGO, former peak found to be red shifted at 270 nm indicates π–π* transition of aromatic C–C bonding as also observed in the FTIR spectra of GO. This shows evidence for redox reaction and also reveals the absence of electron restoring in conjugation of graphene (Gurunathan et al. 2015; Fan et al. 2016b). Bandgap energies are estimated by employing the Tauc relationship, as shown in Fig. 5b–e:

$$\alpha h\nu = K\left(h\nu - E_g\right)^n, \tag{9}$$

where α is absorption coefficient equal to 2.303 log(T/d) (T is transmission of light and d indicates thickness of sample), h represents Planck's constant, ν is light frequency, K is absorption index, and E_g is bandgap energy (eV). The value of exponent (n) is associated with electronic nature of bandgap and corresponds to direct allowed transitions (1/2), indirect allowed transitions (2), direct forbidden transitions (3/2), and indirect forbidden transitions (3), respectively. However, transition data allows to best linear fit in band edge area if $n = 1/2$. Bandgap energy (E_g) is characteristically measured by assessment of $(\alpha h\nu)^{1/n}$ vs $h\nu$ plots. Linear trend acquired from Eq. 9, modeled as the tangent of Tauc plot near the point of maximum slope. If the plot covers an appropriate amount linear area, the linear tangent is extrapolated at a point, where $(\alpha h\nu)^{1/n}$ is equal to zero (or a small value) provided by demonstrated baseline signal (Suram et al. 2016; Viezbicke et al. 2015). Bandgap of GO and rGO was found to be 4.0 and 3.8 eV, respectively, as shown in Fig. 5b, c (Yaragalla et al. 2016; Mangalam et al. 2019).

In UV–Vis spectra of MoS_2, characteristic absorption spectra were observed around 300 nm. MoS_2 nanopetals exhibit increased light absorption in the range below 350 nm for band to band electron transitions and maximum absorption due to intrinsic narrow bandgap and multilayer structure, as shown in Fig. 5a. This phenomenon can be associated with an exclusive production of MoS_2 nanosheets (Pineda-León 2018; Ali et al. 2019). These outcomes corroborate the value of bandgap of MoS_2 which was measured at 2.6 eV, as shown in Fig. 5d (Pineda-León 2018).

In Fig. 5a, spectra obtained from BN indicate the presence of absorption at 210 nm which lies in deep ultraviolet (DUV) region. No other absorption peak at a lower or higher energy side was detected, which reveals the existence of dense structural defects (Kumar et al. 2016; Mahdizadeh et al. 2017). Exfoliated BN-NS exhibit bandgap energy (E_g) of 5.76 eV which supports the direct nature of the bandgap.

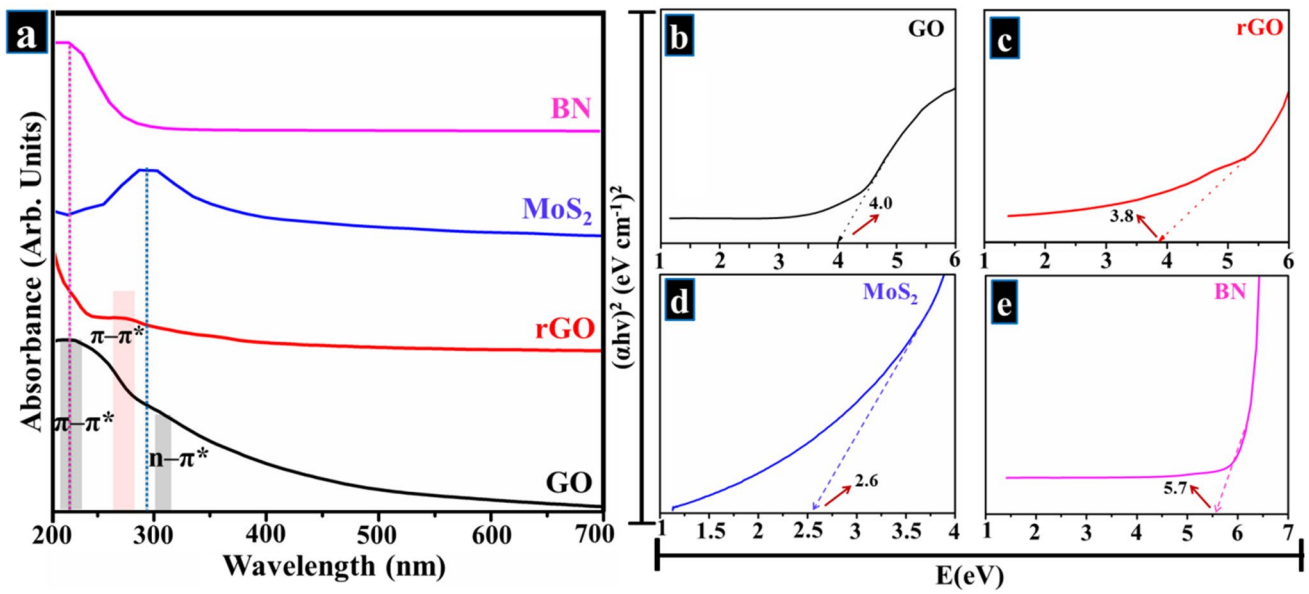

Fig. 5 UV–Vis spectra of prepared species. **b–e** Bandgap of respective samples using Tauc plot

This nature of E_g is due to improved interaction of dispersed layers in electronic bands (Cassabois et al. 2016). This DUV luminescence and extensive bandgap properties make BN-NS a suitable candidate in UV, DUV and photon emission detectors. According to the literature, bulk BN display bandgap values in the range of 5.2–5.4 eV, while in case of bi- or multilayer nanosheets, it is 5.56–5.92 eV (Fig. 5e). In addition, monolayer indicates an E_g value of 6.07 eV which correlates well with theoretical predictions (Zhang et al. 2017b).

The surface morphological features were visualized by FESEM, as shown in Fig. 6a–d. GO sample exhibited thin fluffy curtain-like morphology as well as rich wrinkle-like sheet structure, as observed in Fig. 6a. In case of rGO, partially folded transparent wave-like nanosheets along with slight fluctuations were observed (see Fig. 6b). This 2D structure is vital in sustaining thermodynamic stability of graphene. The surface morphology of MoS_2 revealed nanopetals-like structure with irregular distribution of petals in Fig. 6c. Several interspaces were visible among nanopetals that appeared to be scattered. FESEM micrograph of BN nanosheets in Fig. 6d indicates that synthesized particles displayed nanosheet-like morphology. Nanosheets are compact with uniform features and curved edges.

HR-TEM was used to gain further information about surface morphology of 2D materials. Figure7a, b reveals morphology of GO and rGO, respectively. Lamellar and sheet-like surface with transparent area was observed in case of GO and rGO (Fig. 7a, b) with a few surface stacking folds due to distortion from a large fraction of carbon bonding defects. Figure 7c unveils morphology of MoS_2 as thin scattered layers composed by a single monodispersed sheet with slight curvature or twist. The corresponding image in Fig. 7c′ shows interlayer spacing of bare MoS_2 calculated by IFFT (inset) with measured spacing of 0.62 nm that corresponds to (002) plane seen in XRD. These findings provide evidence for the formation of 2H structure of MoS_2 (Veeramalai et al. 2016; Wu et al. 2010). Image in Fig. 7d shows dark and bright segments in TEM image, which correspond to variation in density or thickness of nanosheets.

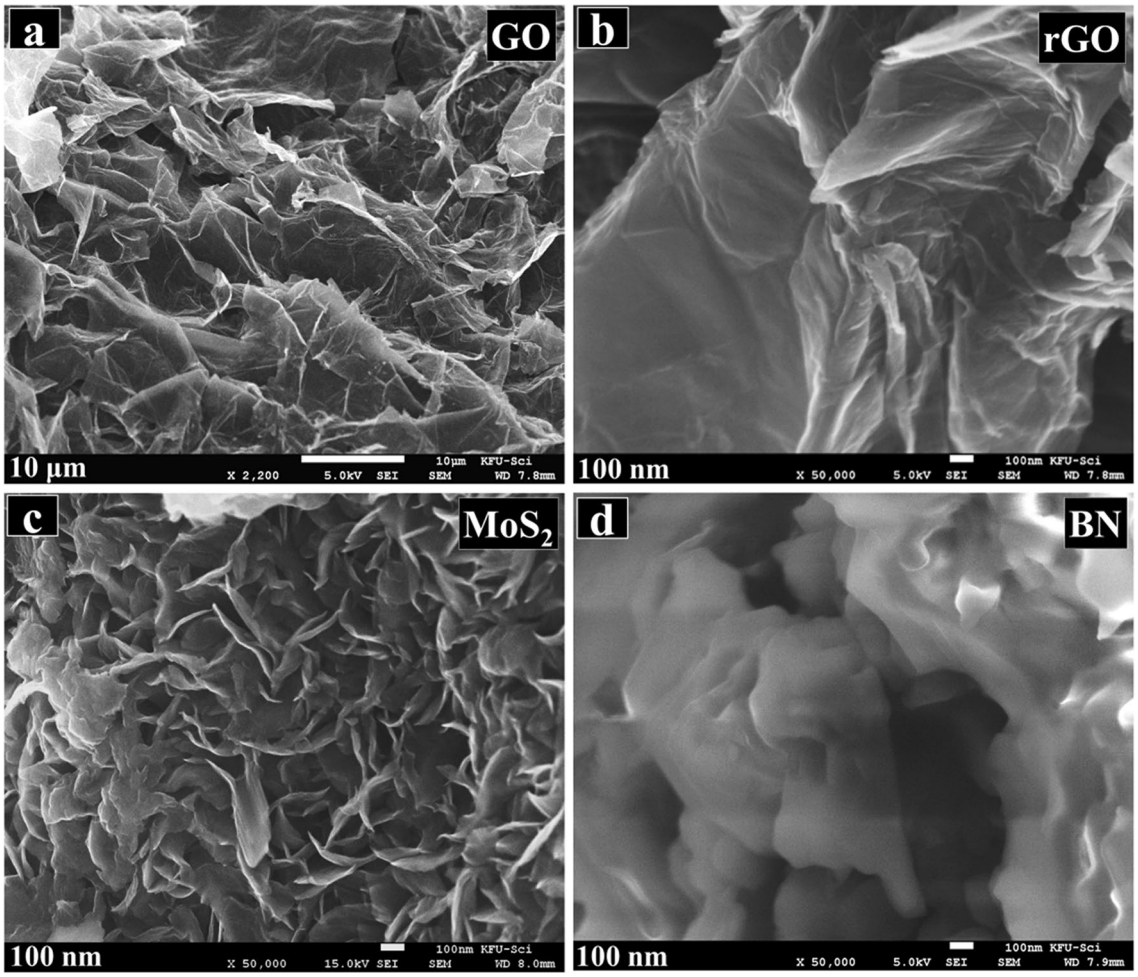

Fig. 6 FESEM images of **a** GO, **b** rGO, **c** MoS_2, **d** BN

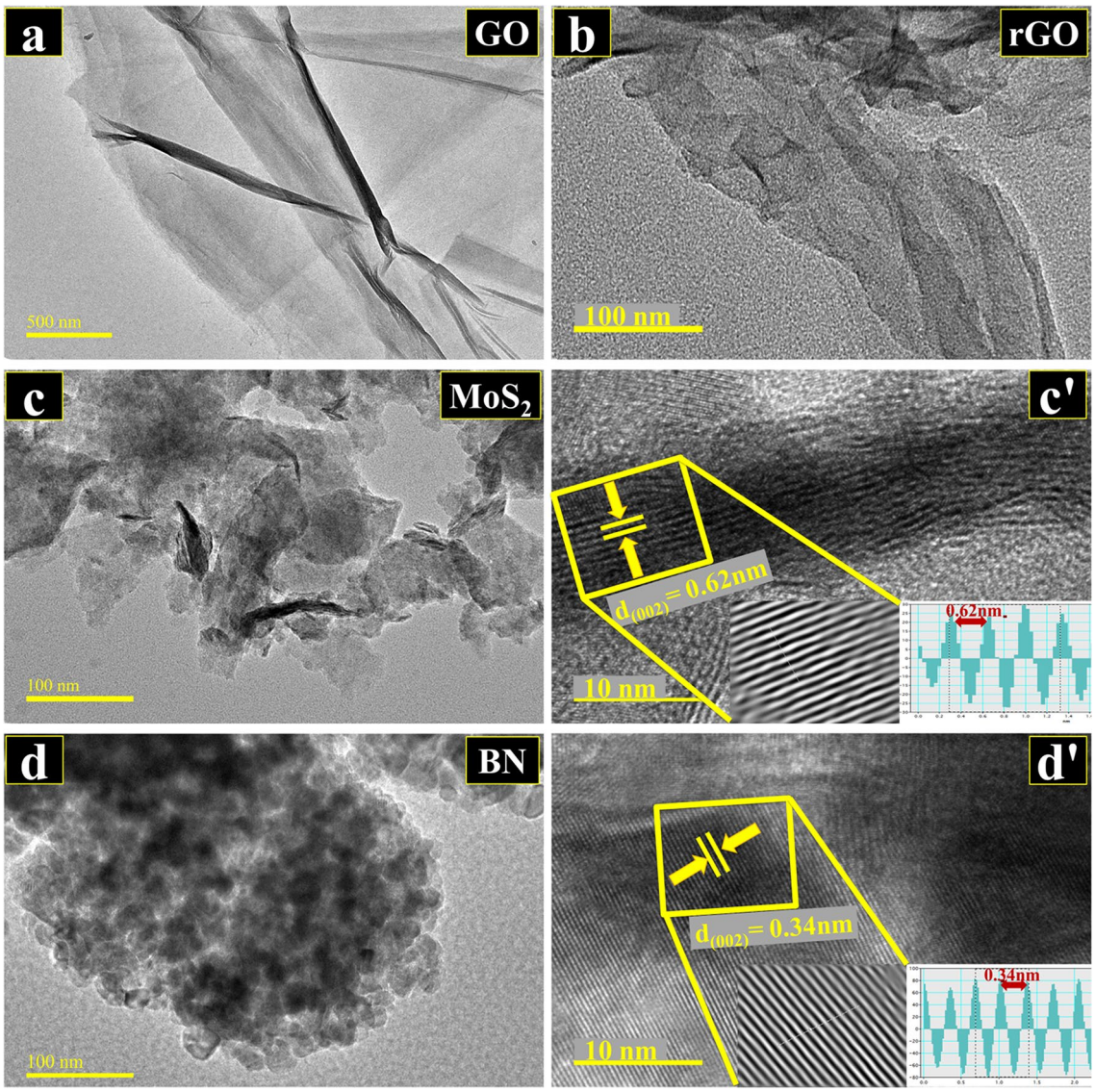

Fig. 7 **a**, **b** HR-TEM images of GO and rGO, **c**–**c**′) 100 nm image of MoS_2 and corresponding 10 nm image used for d-spacing measurement (**d**–**d**′) 100 nm image of BN and corresponding 10 nm image used for d-spacing measurement

The sheet-like morphology observed in the samples during TEM investigation is a result of chemical exfoliation process. Evidently, observed morphology of prepared samples demonstrates that chemical exfoliation had no adverse effect on shape and structure of nanosheets. Corresponding image in Fig. 7d' reveals that the interlayer distance of h-BN at d_{002} is 0.34 nm which agrees well with the XRD pattern of pure BN (Ji et al. 2012; Zhong et al. 2017).

Raman spectroscopy was used to determine molecular vibrational mode and structural fingerprint by which molecules can be identified further. Raman spectroscopy provides information about the number of layers and density of defects of low dimensional structures, as illustrated in Fig. 8a–d. In the Raman study of GO (Fig. 8a), two characteristic bands are observed at ~ 1360 and 1593 cm^{-1}. Comparatively, in rGO, D and G bands exist at ~ 1338 and 1583 cm^{-1}. Progressive features in Raman spectra of graphene and their analogs are peak positions as well as intensity of G and D bands and their overtones (2D) (Tiwari et al. 2017). The G band is indicative of sp^2 hybrid structure which signifies crystallizability and symmetry of carbon atoms as well as introduction of scattering phonon mode (E_{2g}). The D band arises due to breathing mode of k-point with A_{1g} phonon mode symmetry, which is also an indication of sp^3 carbon atoms (Gurunathan et al. 2015; Fan et al. 2016b; Haldorai et al. 2014; Gong et al. 2015). In addition, D band is a measure of surface defects and imperfections in structures that appear with attached hydroxyl and epoxide

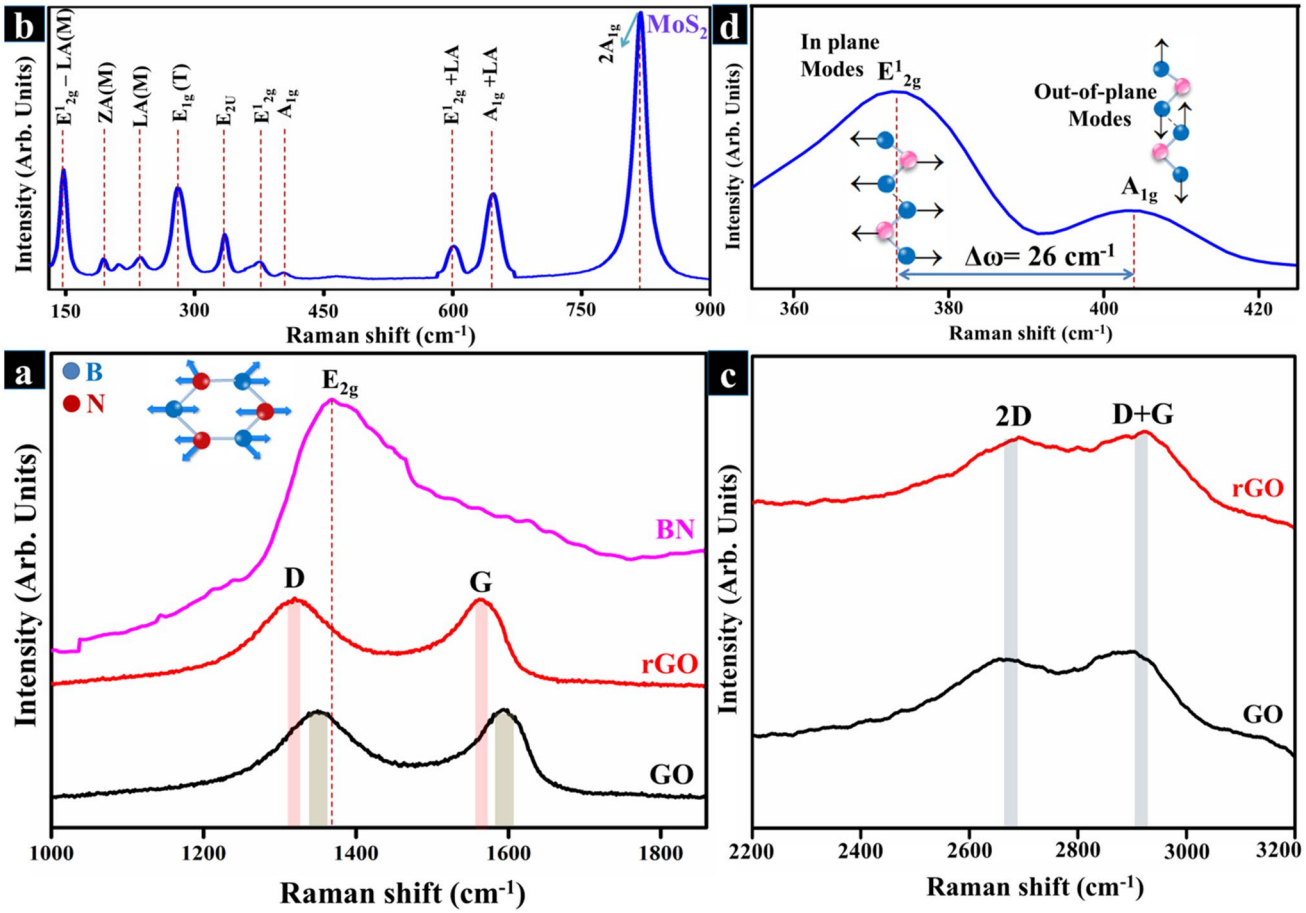

Fig. 8 **a** Raman spectra of GO, rGO and BN, **b** MoS_2, **c** zoom area of 2D and D + G bands of GO and rGO, **d** magnified area of characteristic peaks of MoS_2

functional groups intercalated between carbon basal planes (Suresh et al. 2018; Gurunathan et al. 2015). Latter band (G) is only present in Raman mode that is initiated by conventional 1st-order Raman scattering process and relates with in-plane zone center. It also doubly degenerates phonon mode [transverse (TO) and longitudinal (LO) optical] with E_{2g} symmetry (Frank et al. 2011). Figure 8c shows other two bands at 2682 (2D) and 2900 cm^{-1} (D + G). The latter band represents slight disordering due to scattering combination (Suresh et al. 2018; Ngidi et al. 2019; Tiwari et al. 2017; Frank et al. 2011; Gayathri et al. 2014). The 2D band is not mentioned nor addressed in several previous studies. 2D (or G′) mode instigates from 2nd order of D band with double resonant process between non-equivalent K points within Brillouin zone (BZ) of graphene. This band occurs due to lattice vibrations of phonons; nevertheless, it is not related to defects such as in D band. Assuredly, 2D band is perceived as a strong band even when there is no existence of D band (Ngidi et al. 2019; Frank et al. 2011; Gayathri et al. 2014). Difference in relative intensities of D and G bands in GO during reduction process typically reveals change of electronic conjugation state. This change proposes an increase in the number of sp^2 atomic domains through GO reduction (Gurunathan et al. 2013). Mostly, 2D band depends upon the scattering rate of electrons or holes with lattice and charge carrier of some doping materials. Consequently, I_D/I_G ratio will increase electron defect elastic scattering rate, whereas I_{2D}/I_G ratio would increase electron–hole inelastic scattering rate referred to as Coulomb interaction (Ngidi et al. 2019). Indeed, intensity ratio I_D/I_G (Fig. 8a) is extensively employed to determine defect quantity in graphene layers; a high ratio indicates a largely disordered structure. The intensity ratio of GO and rGO is ~ 0.80 and ~ 0.91 respectively, which confirms the reduction in average size of sp^2 atomic domains along with edge defects as a result of C=C bond reduced in GO (Ding et al. 2018b; Yasin et al. 2018; Kaniyoor and Ramaprabhu 2012).

In acquired Raman spectrum of MoS_2, detectable peaks are sited at 146, 188, 231, 285, 338, 375, 401, 600, 645, and 820 cm^{-1} which agrees well with the literature, as demonstrated in Fig. 8b (Ahmed et al. 2018; Placidi et al. 2015; Windom et al. 2011; Demas et al. 2012; Thangappan et al.

2016). In the plotted spectrum, three 1st order active modes occur at frequencies of 285, 374 and 401 cm^{-1} allocated as E_{1g}, E^{1}_{2g} and A_{1g} vibrational modes, respectively which suggests the formation of 2H phase of MoS_2 (Windom et al. 2011; Demas et al. 2012; Thangappan et al. 2016; Sun 2016). The E_{1g} mode is prohibited on a basal plane in a back-scattering experiment according to Raman tensor and basically, this mode is originated by S–Mo–S interlayer vibrations (Ahmed et al. 2018; Demas et al. 2012; Sun 2016). The E_{2g} vibrational mode is related to in-plane vibrations of S atoms with respect to Mo atoms. Besides A_{1g} mode specifies out-of-plane vibrations caused by two S atoms vibration with opposite direction to Mo stationary atom, as demonstrated in Fig. 8d (Sun 2016; Liu et al. 2016). Frequencies of these two modes (E_{2g} and A_{1g}) reveal layered features of S–Mo–S. Generally, these two modes are commonly used to recognize the number of layers (N) of MoS_2, which are directly related to the frequencies of these modes (Sun 2016; Mouri et al. 2013; Patil et al. 2014; Lewandowska 2014; Bozheyev et al. 2017). Accordingly, in-plane (E_{2g}) and out-of-plane (A_{1g}) vibrational modes exhibit opposite variation trend toward decreasing number of layers in S–Mo–S, which suggests prevalence of E_{2g} vibration mode under A_{1g} mode due to the weakening of van der Waals forces that exist in adjacent layers (Sun 2016; Bozheyev et al. 2017). Subsequently, frequency difference between E_{2g} and A_{1g} is ~ 26 cm^{-1} which suggests formation of 6L, as displayed in Fig. 8d (Thangappan et al. 2016; Sun 2016; Mouri et al. 2013; Lewandowska 2014). Some other peaks around 146 and 188 cm^{-1} are ascribed to E_{2g}—LA(M) and ZA(M) phonon mode, respectively (Placidi et al. 2015; Windom et al. 2011). Vibrational mode at 231 cm^{-1} is referred to first-order LA(M), which occurs with a disorder in induced scattering from zone edge M point (Sun 2016). Peak at 645 cm^{-1} is a combination of LA(M) and A_{1g} mode; another intense peak around 820 cm^{-1} is accredited to 2nd order spectral region in Raman scattering ($2A_{1g}$), as shown in Fig. 8b (Windom et al. 2011; Gołasa et al. 2014).

Raman spectra of BN display a strong peak positioned at 1367 cm^{-1} which refers to E_{2g} active phonon mode (Fig. 8a). This E_{2g} mode can also be attributed to G band of 2D-graphene as boron nitride is a graphene analogous 2D material (Li et al. 2014; Cai et al. 2017; Feng and Sajjad 2012). Explanation of this G band was included in Raman analysis of grapheme, while illustration of this band is visualized in Fig. 8a. Few layered nanosheets cause slight elongation within boron and nitrogen bonds (B–N). Consequently, this elongation in B–N bond indicates the softening of phonons and agrees well with previously cited results (Thangasamy and Sathish 2015; Kumbhakar et al. 2015). Over a few layers, monolayer h-BN induces expected shortening of B–N bond owing to weak van der Waals forces among interlayer interaction (Lee and Song 2017). Literature studies reveal that high-quality monocrystal h-BN exhibits E_{2g} active phonon mode at 1367 cm^{-1} (Weng et al. 2013). Generally, Raman spectra of BN are subordinate to phonons (lattice vibrations) which are strongly affected by chemical structure together with atomic bonds of supported material (Singh et al. 2016). Broadening of E_{2g} mode was detected which may be caused by ordering of stacked layers, domain size or porosity present in the material (Mahdizadeh et al. 2017). Moreover, two minor peaks in Raman spectrum were also observed around 500 and 800 cm^{-1} that originate due to high florescent background or may be due to amines (Štengl et al. 2014).

Photoluminescence (PL) spectroscopy was undertaken to probe migration and recombination of electron–hole pairs as well as interaction between graphitic 2D nanostructures. Recombination of e^-/h^+ generates photonic emission resulting in photoluminescence phenomenon, as illustrated in Fig. 9a (Bano et al. 2019; Pal 2015). In case of graphite, no luminescence behavior was observed due to of its zero bandgap, though at nano-level bandgap became wide owing to quantum confinement effects as shown by the observed results of luminescence phenomenon (Ding et al. 2018b). With regard to the optoelectronic properties of carbon-based materials, sp^2 and sp^3 both are bonded zones and directed by π sp^2 state of atomic domains. A fixed ratio of π and π^* energy states of sp^2 domains exists in between σ and σ^*, respectively, of sp^3 matrix. Disordered carbon film contains both regions (sp^2 and sp^3), and therefore, PL through these materials attributable to radiative recombination of e^-/h^+ pairs confined in sp^2 domains. The emitted photon can be organized by changing sp^2 cluster shape, size and fraction. This photoemission can be organized by changing fraction, size and shape of sp^2 clusters (Pal 2015). In further research regarding GO and rGO nanosheets, oxide functional groups and empty states of carbon can alter graphene into many nano-carbon clusters that show luminescence and semiconductor behavior (Ding et al. 2018b; Bano et al. 2019). In acquired spectrum, observable peaks were detected around ~ 330, 565 and 608 nm elucidating recombination of electron–hole pair in sp^2 confine state of carbon clusters combined using sp^3 matrix. Consequently, rGO luminescence is disturbed through disappearing of functional groups associated with oxygen that facilitate percolation of paths among sp^2 clusters (Ding et al. 2018b; Bano et al. 2019; Jayanti et al. 2017).

In Fig. 9a, PL spectra of MoS_2 monolayer show the behavior of a direct bandgap, where inter band transition of lowest energy semiconductor at Brillouin zone of K-point. Emitted photon with 1.9 eV energy occurred due to excitons relaxation at K-point (Eda et al. 2011). As expected, through partial metallic character bulk MoS_2 do not exhibit PL spectrum. The emission spectra for MoS_2 single layer consist of two characteristics peaks of one at 610 and the

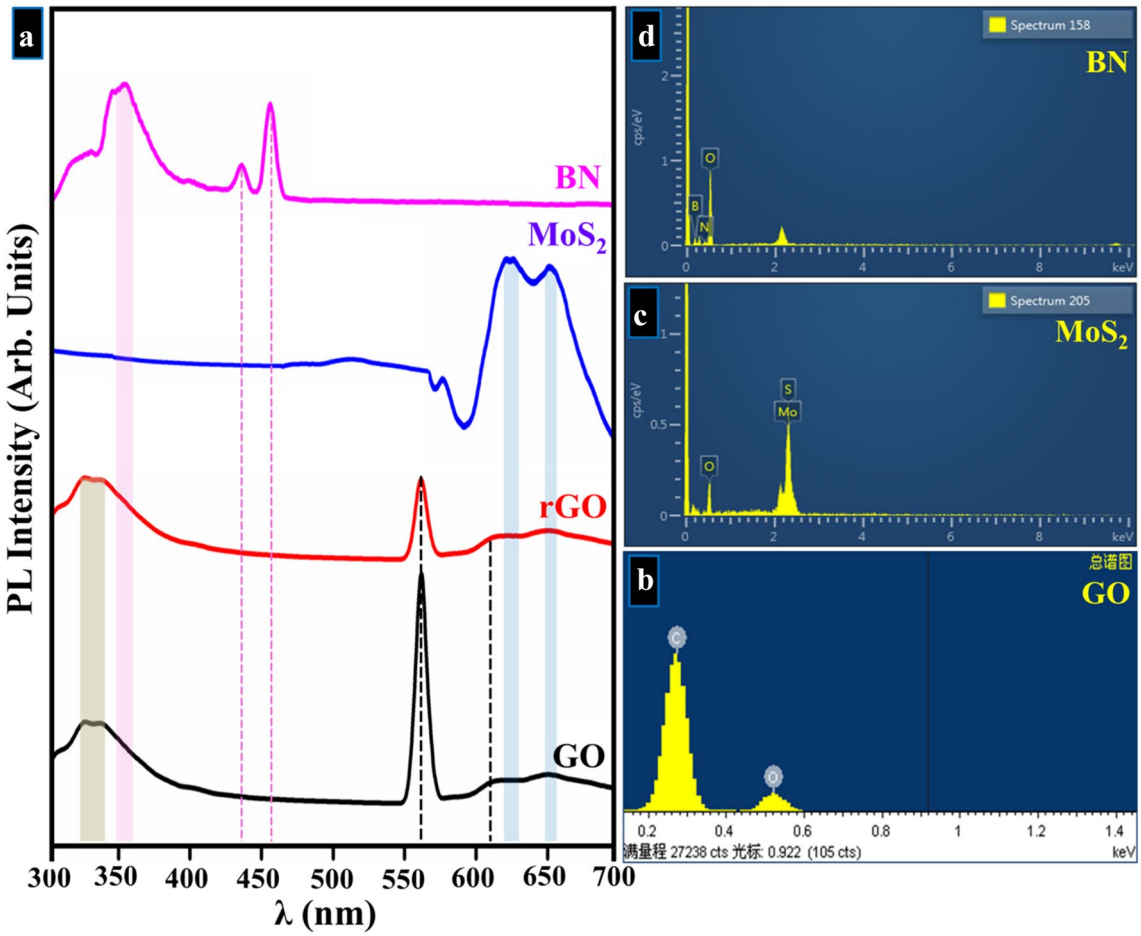

Fig. 9 **a** PL spectra, **b–d** EDS profiles of respective samples

other at 660 nm. These peaks are to be regarded as A and B that are well consistent with A and B excitons energy leading to PL direct gap as of K-point (Raza et al. 2019; Chacko et al. 2019). Mechanically exfoliated MoS_2 monolayer corresponding to the observed PL spectra forms due to intrinsic properties of MoS_2 and has no interaction with structural defects or impurities. Defects using Mo and S unsaturated bonds that originate from midgap-state are directed as active non-radiative recombination centers for excitons (Eginligil et al. 2015).

PL spectra of BN nanosheets display a wide band identified at ~ 330 nm (blue emission) that corresponds to vacancies present, which can be optimized as excitons recombination, adsorption, activation, and photosensitivity centers (Fig. 9a) (Lee and Song 2017). In addition, PL spectra exhibit onset of luminescence at ~ 460 nm which could be attributed to the commencement of electronic transition. Surely, this electronic transition includes individual/mutual transition among 2p states of BN bands (Doll et al. 1989). Excitation of an electron (e^-) from lower to higher (valance to conduction) band causes to boost luminescence intensity as well as an enhancement in the energy of excitation light. This electronic transition (460 nm) represents the presence of an energy peak ~ 2.7 eV (Wu et al. 2017). The most intense peak implies maximum recombination of photogenerated charges, where the lowest intensity indicates separation of electron holes (Silly et al. 2007). K. Watanabe et al. (Watanabe and Taniguchi 2009) reported Jahn–Teller effect on excitons state in h-BN consistent of distortion in excited state (E_{2g} type). Moreover, expression of Jahn–Teller for phonons at Brillouin zone center can be expressed as

$$2E_{1u} + 2A_{2u} + 2E_{2g} + 2B_{1g}.$$

According to Jahn–Teller effect, two types of E_{2g} modes are probable in removing degeneracy of excitons states. Firstly, phonon mode of shearing among two facing sp^2 layers that constitutes B and N atoms. Secondly, possible E_{2g} mode in which both B and N atoms (in-plane) move in opposite path as facing atoms move in the same segment among layers (Watanabe and Taniguchi 2009). The emission spectra acquired in this study indicated an excitation supported PL

behavior that is in agreement with the reported literature (Liu et al. 2019b).

EDS was employed to identify elemental composition of all prepared samples. Image in Fig. 9b shows GO composition as carbon and oxygen is detected only. There is no peak from impurities which is evident to the formation of pure GO. Figure 9c confirms the presence of Mo and S atoms indicating the presence of MoS_2. Oxygen peak is generated due to pick-up of oxygen during synthesis (Li et al. 2019). Figure 9d indicates strong signals for boron and nitrogen atoms which suggest formation of as-prepared product. In addition, an artificial signal of oxygen is also detected in EDS which may arise due to the impurity of fluorescent background.

XPS analysis is used for quantitative surface analysis specifically, to determine chemical as well as electronic state, corresponding empirical formula, and more importantly elemental composition (Khanra et al. 2012). In the present study, XPS was undertaken to detect presence of oxygen-related functional groups associated with GO. The high-resolution XPS survey of GO in Fig. 10a shows that GO displayed significant C 1 s and O 1 s peaks attributed to the binding energy of GO (Fig. 10b, c). Peak assignment in O 1 s spectra supported assignments of "carbon, oxygen" functional groups as discussed in the literature. Information obtained from O 1 s analysis can be combined with the information provided by C 1 s analysis. Photoelectron kinetic energies in O 1 s spectra are smaller than those recorded in C 1 s. O 1 s spectra reveal a somewhat larger specific surface, since sampling depth is lower. The O 1 s peak positioned at 530.6 eV originate from C=O, while O=C–OH groups and peak identified around 533 eV corresponds to C–OH groups, as can be seen in Fig. 10b (Yang et al. 2009). Figure 10c indicates the presence of a significant peak of C 1 s with a binding energy of ~ 284.0 eV that can be assigned to graphitic C–C peak owing to sp^2 carbon bond and oxygen-containing functional groups (Jiang et al. 2013). Two clear peaks C 1 s appear at binding energies of 285.7 and 288.0 eV that can be associated with C–O and C=O (carbonyl C), respectively. Clearly, most of the oxygen-containing functional groups in GO are epoxide groups (C–O–C) (Ren et al. 2011; Krishnamoorthy et al. 2013).

XPS spectra were acquired to determine chemical state of Mo and S within MoS_2, as indicated in Fig. 10d, e. In

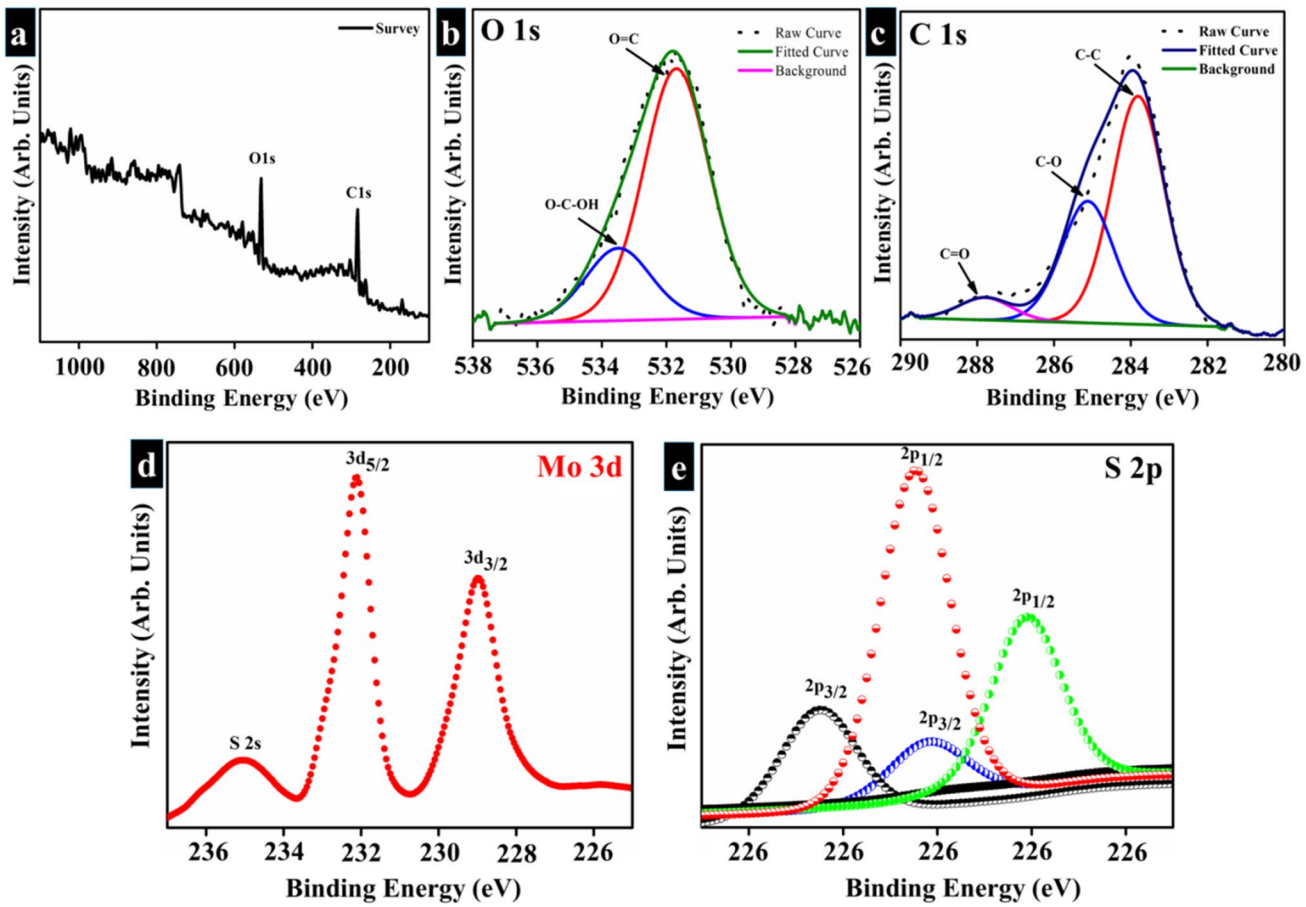

Fig. 10 XPS spectra. **a**–**c** GO and **d**–**e** MoS_2

Fig. 10d, high-resolution XPS data provide information about Mo $3d_{5/2}$ and Mo $3d_{3/2}$ binding energies which corresponds to 229.88 and 233.03 eV, respectively, pointing toward the presence of Mo^{+4} in pure MoS_2 (Qumar et al. 2020; Ke et al. 2017). Besides S, an apparent peak positioned at 226.8 eV is attributed to the binding energy of S 2 s, which suggests the presence of MoS_2. Whereas in Fig. 10e, a spectrum of S 2p region with single doublet peaks of $2p_{3/2}$ (161.7 eV) and $2p_{1/2}$ (162.8 eV) confirm Mo–S bond. Similarly, peak at 163.0 eV and 163.9 eV can be assigned to S $2p_{3/2}$ and S $2p_{1/2}$ is attributed to S element spin–orbit separation, suggesting the presence of −2 oxidation state of S (Qumar et al. 2020; Ali et al. 2019; Vattikuti et al. 2015).

The thermal behavior of GO was measured up to 1000 °C through DSC/TGA measurements. In Fig. 11a, small but far from negligible endothermic peak of GO was observed before 100 °C, which significantly corresponds to desorption of water (Traina and Pegoretti 2012). Another endothermic peak of GO is evidenced at 213 °C which points toward GO thermolysis, after which weight loss becomes smoother (Lu et al. 2013). In TGA curve (Fig. 11a), initially GO loses about 20% mass below 100 °C owing to water evaporation and pyrolysis of oxygen-containing –OH, COOH groups, etc. As temperature is increased, mass loss becomes very rapid, initial mass loss of roughly 30% occurs at a temperature of about 200 °C indicating thermal decomposition of functional groups associated with oxygen. This is presumably, owing to pyrolysis of oxygen-related functional groups, e.g., hydroxyl (–OH), carbonyl (COOH) and carboxylic-acid (RCOOH) yielding CO, CO_2 and water molecules (H–O–H) (Alam et al. 2017; Wang et al. 2012a). Around this temperature, GO is effectively converted into conductive (rGO). In case of GO sample, rapid mass loss around initial/starting temperature specifies higher defect density (Alhassan et al. 2013).

DSC-TGA analysis was performed in an air environment to investigate the phase transformation of MoS_2,

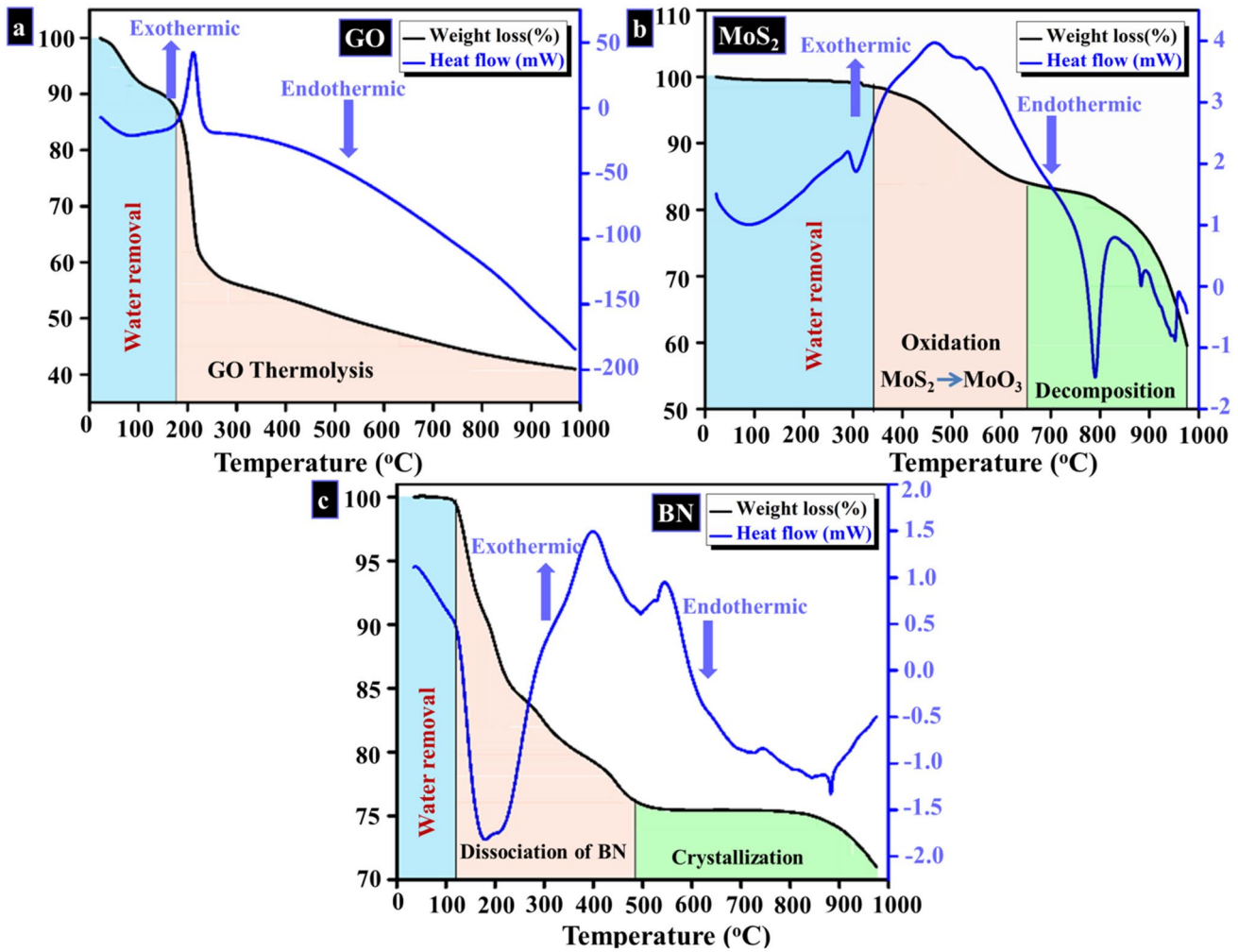

Fig. 11 DSC-TGA curves. **a** GO, **b** MoS_2 and **c** BN

as shown in Fig. 11b. Prepared samples were exposed to temperature ranges from 25 to 970 °C keeping ramp rate of 10 °C/min. TGA analysis indicates that initial weight loss of 2–3% starts at 330 °C, most probably attributed to removal of water as hydronium ion (H_3O^+) as explained by Eq. 10 and organic material content used for washing samples during synthesis. Further weight loss can be explained with the following reaction:

$$HCl + 2H_2O \rightarrow H_3O^+ + Cl^-. \quad (10)$$

In Fig. 11b, an exothermic peak observed at 514 °C may correspond to oxidative roasting of molybdenite (Raza et al. 2019; Golmakani et al. 2018). Main factors that influence the formation of this exothermic peak could be MoS_2 partial oxidative roasting phenomenon. Furthermore, the formation of this exothermic peak can be elucidated with the help of Eq. 11:

$$MoS_2 + 3.5O_2 = MoO_3 + 2SO_2 + Q \quad (11)$$

It is important to mention that DSC results presented in the range of 100–200 °C in Fig. 11b do not indicate any thermal peak, aside from a partial detachment. However, mass loss with fairly significant peak demonstrates physical transformation within this range of temperature. Another 2–5% weight loss observed at 795 °C reveals thermal decomposition of MoS_2 (Nafees et al. 2015). The reaction takes place under a temperature of 800–1100 °C, at this temperature MoS_2 (VI) decomposes into molybdenum (III) sulfide and sulfur.

Chemical reaction for thermally decomposed MoS_2 is given by Eq. 12 as follows:

$$2MoS_2 \left(\begin{matrix} 800-1100°C \\ \rightarrow \end{matrix} \right) Mo_2S_3 + S. \quad (12)$$

Figure 11c represents DSC-TGA curve of BN-NS measured from room temperature to 1000 °C. Some endothermic peaks were identified on DSC curve around 220, 450, and 880 °C. These peaks correspond to dissociation, melting, solidification, and crystallization, respectively. Peaks around 220 and 450 °C are attributed to phase transformation from bulk BN to BN nanosheets (Grossman et al. 2016). Correspondingly, TGA curve indicates two decreases in gravity. First decrease in gravity is identified at the start of temperature rise from ~ 120 to 490 °C, which can correspond to a loss of surface adsorbed/functionalized water as well as organic groups resulting from the presence of ionic B–N bonds. The second decrease in gravity is detected at ~ 850 °C which corresponds to the formation of BN–NS (Wang et al. 2012b, 2016b). No weight loss was observed below 120 °C and in the range 450–850 °C, which stems from thermal stability (Wang et al. 2016b).

In Fig. 12, both photocatalysis and sonophotocatalysis are described simultaneously. The light-induced activity of all samples is illustrated in Fig. 12a, b for PCA, where absorbance is displayed as a function of time. Photocatalytic response of all 2D materials arise due to their high surface area. In Fig. 12a, maximum degradation is shown by rGO with C/C_o equal to 0.39 (60%) concentration within 120 min. Small amount of degradation occurs in all samples in the dark but during the presence of light, samples demonstrate substantial MB removal within 120 min. Moderate degradation is displayed by MoS_2 with C/C_o equal to 0.44 (55%) owing to its small bandgap, while BN shows less degradation because of its wide bandgap. Figure 12b, c shows SPCA plot with similar calculations which reveals a significant increase in dye reduction, when samples were placed in an ultrasonic bath.

Rate constants of all samples using the pseudo-first-order equation is given as (Eq. 13) (Arshad et al. 2017)

$$-\ln\left(C_t/C_o\right) = kt, \quad (13)$$

where C_t is the concentration at a specific time and C_o is the initial concentration, k is an apparent rate constant. Figure 13a, b shows that PCA and calculated rate constants for rGO, MoS_2, GO, and BN are 0.0076, 0.0068, 0.0041 and 0.0033 min^{-1}, respectively. Figure 13c, d shows SPCA rate constants and % degradation calculated as 0.0178, 0.0118, 0.0086, and 0.0051 min^{-1} for rGO, GO, MoS_2, and BN, respectively. Figure 13a, c shows baseline C that represents ratio of C_t/C_o. Figure 13b, d reveals % degradation of all samples with time. These findings show strong potential of rGO to treat industrial wastewater. Significant enhancement in photocatalytic efficiency was observed due to doping of materials. Results show that SPCA is more efficient than simple PCA suggesting that reduction can be enhanced by incorporating dopants. Literature survey reveals that incorporation of dopants into 2D materials causes to accelerate dye degradation as well as increase its efficacy. Various reports reveal maximum dye reduction with doping of selected species into host rGO, GO, MoS_2 and BN (Kumar et al. 2019; Hassan et al. 2020; Tian et al. 2016; Sheng et al. 2019; Ikram et al. 2020d). Comparison of degradation results with those previously reported are shown in Table 1.

pH value

In PCA and SPCA, pH value plays a vital role during dye degradation treatment of textile wastewater, especially in reaction mechanisms that can contribute to dye degradation. Percentage degradation as calculated using Eq. 1 has a direct relation with pH value. In the currently performed experiments for BN, MoS_2, rGO and GO, value of pH was recorded as 8.5, 9.1 8 and 8.2, respectively which clearly

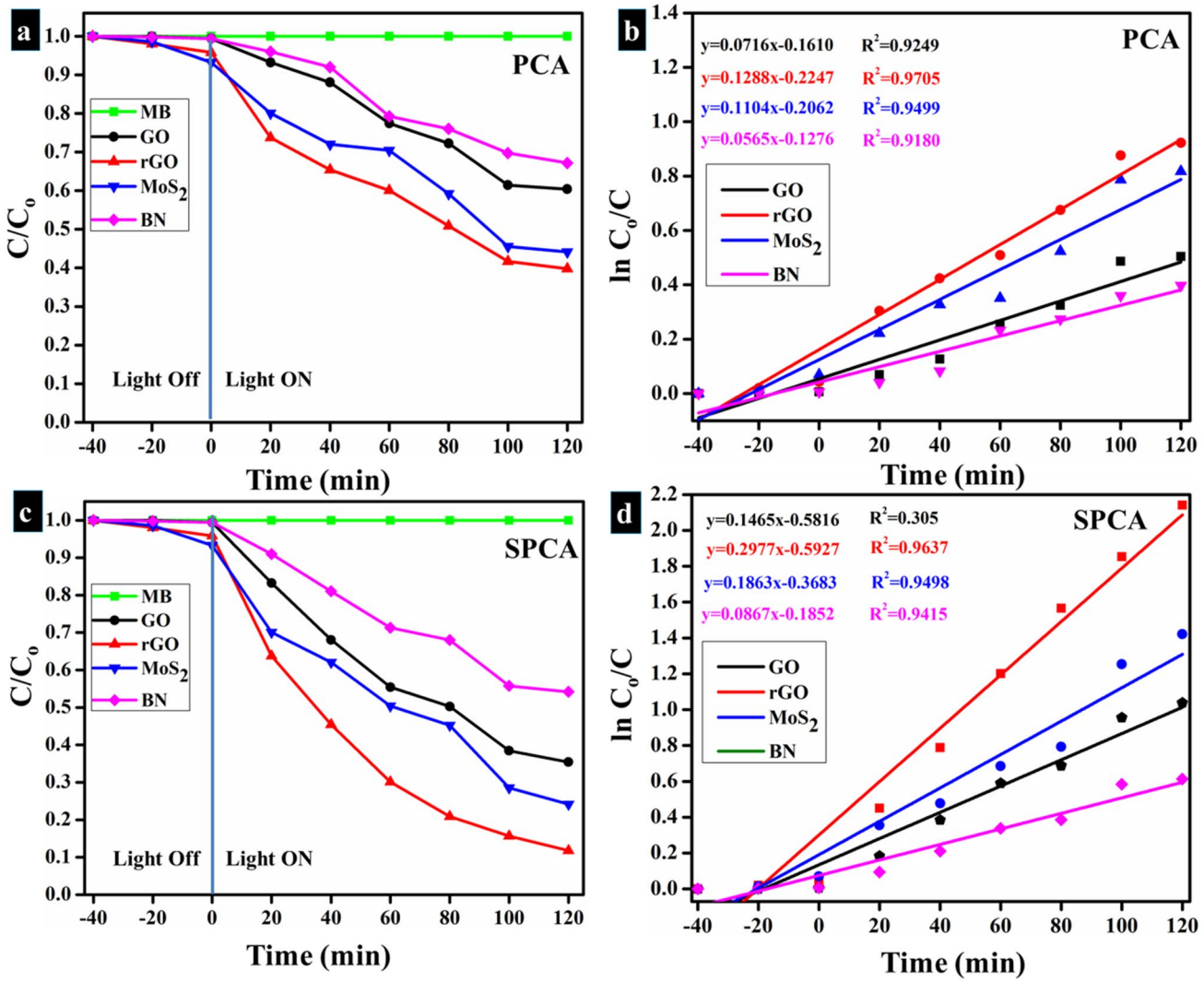

Fig. 12 **a**, **b** Plot of concentration ratio (C/C_0) vs time and plot of $-\ln(C_t/C_0)$ vs time spectra for sonophotocatalysis. **c**, **d** Plot of concentration ratio (C/C_0) vs time and plot of $-\ln(C_t/C_0)$ photocatalysis

indicates experiment was carried out in a basic environment. In addition, dye degradation using photocatalytic approach shows excellent results under basic conditions that constructively support the findings of this study.

Stability and reusability

Since the stability of PCA and SPCA is an important factor in the performance assessment of a photocatalyst, the stability and reusability of experiments performed in this study were investigated. Performed experiment for all samples was allowed to stay for 3 days in dark after 120 min of irradiation. After 3 days, it was observed that the degradation was still in its previously observed form. Discoloration of dye was still the same as was performed initially. Reusability was examined by recycling of rGO (Fig. 13a, c) and MoS_2 (Fig. 14b, d) as these two catalysts exhibited superior dye degradation compared to other synthesized materials. Recycling of photocatalyst was performed for up to four cycles which showed approximately the same results when compared with the actual experiment. It can be seen from the above two experiments that SPCA resulted in efficient and enhanced dye degradation as compared to simple PCA. Obtained spectra for recycling of photocatalyst were also monitored through UV–Vis, as visualized in Fig. 14a–d.

Load of photocatalyst

Load of catalyst also holds great importance with regard to testing dye degradation for a number of cycles. In the above executed experiment, load of photocatalyst before and after four cycles of recycling was observed.

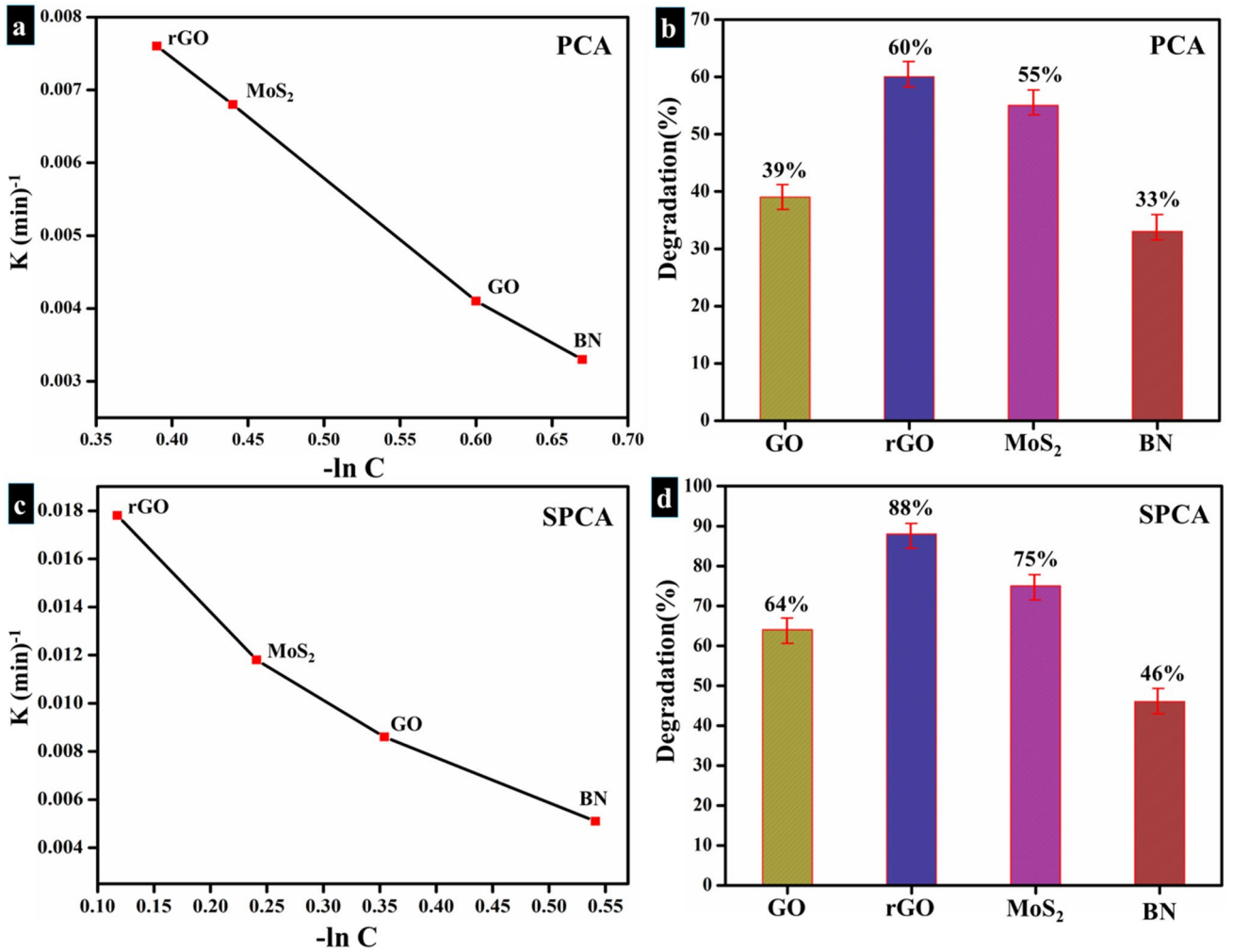

Fig. 13 **a**, **b** Rate constants and degradation (%) of PCA, respectively. **c**, **d** Rate constants and % degradation for SPCA, respectively

Table 1 Comparison of degradation of MB with reported results

Sample	Literature Degradation (%)	Present study Degradation (%)
GO	62 (Ikram et al. 2020b)	64
rGO	65 (Deng et al. 2016)	60
MoS_2	45 (Yein et al. 2019; Phung et al. 2018)	55
BN	30 (Sheng et al. 2019)	33

Minor weight loss was detected for both rGO and MoS_2. For MoS_2 and rGO weight of actual photocatalyst was 10 mg prior to experiment. After four cycles, it decreased down to 9.4 mg taking into consideration ~ 5% sensing deviation.

Conclusion

In the present study of comparison of 2D materials, GO was synthesized using revised Hummers method and reduced GO was extracted from GO using thermal reduction technique. MoS_2 nanopetals and BN nanosheets were synthesized via hydrothermal and chemical exfoliation strategies, respectively. XRD was used to detect hexagonal phase present with all samples and calculate inter-layer spacing which coincided well with HR-TEM micrographs as well as confirmed the reduction of GO. Fingerprint region of sp^2 hybridized carbon was sited at 650 cm^{-1} and assigned to C–H, which is an evidence for the formation of Dirac 2D material. The characteristic peak of Mo and S bonding was located around 676 and 1124 cm^{-1}, respectively, and characteristic modes E_{1u} and A_{2u} of BN were assessed through FTIR. UV–Vis spectra revealed π–π* transition in aromatic C–C and n–π* transitions for GO and rGO. It was also used to calculate bandgap of GO (4.0 eV), rGO

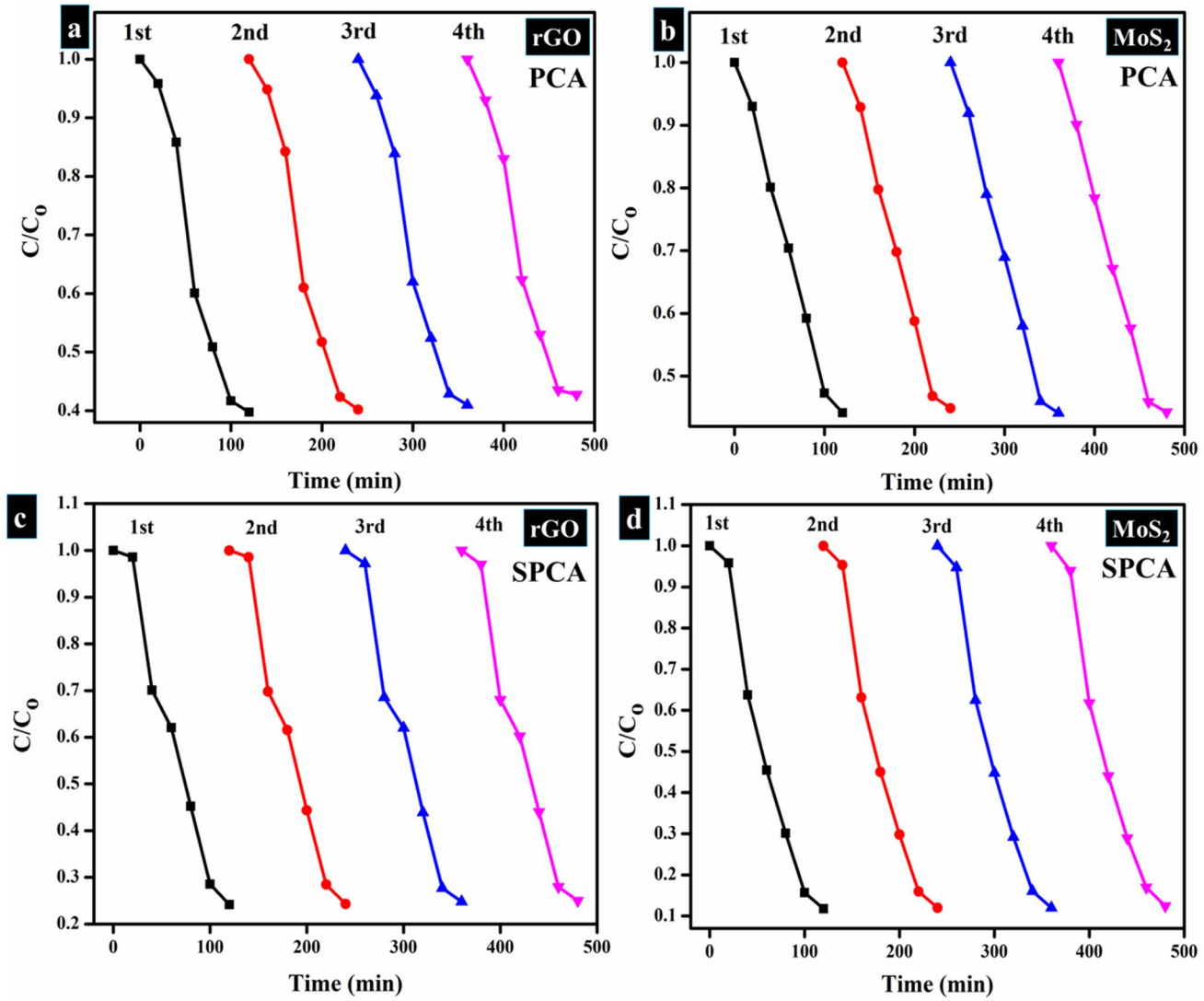

Fig. 14 **a**, **b** Plots of C/C_0 vs time for reusability for PCA of rGO and MoS_2, respectively, **b**, **c** reusability for SPCA of rGO and MoS_2 reusability

(3.84 eV), MoS_2 (2.6 eV) and BN (5.7 eV). FESEM and HR-TEM micrographs revealed transparent nanosheets with slight fluctuation and thin fluffy curtain-like morphology as well as rich wrinkle-like structure observed in GO and rGO, and dispersed MoS_2 nanopetals with interlayers spacing of 0.62 nm. BN nanosheets possessed a d-spacing of 0.34 nm as visualized with HR-TEM. In Raman studies, G band indicated sp^2 hybrid with crystallizability and symmetry of carbon atoms along scattering phonon mode (E_{2g}). D band indicated k-point breathing mode with A_{1g} phonon mode symmetry which is also an indication of sp^3 carbon atoms. Two other bands at 2682 (2D) and 2900 cm^{-1} (D + G) were detected. The D + G band represents slight disordering due to scattering combination. In case of MoS_2, E_{2g} vibrational mode was related to in-plane vibrations and A_{1g} mode was identified as out-of-plane vibrations. Frequency difference between E_{2g} and A_{1g} was ~ 26 cm^{-1} that suggests formation of six layers. Besides, in BN, E_{2g} mode was attributed to G band that is analogous to graphene, and a few layered structures that caused slight elongation within boron and nitrogen bonds (B–N). In case of GO and rGO, PL spectra were attributed to recombination of electron–hole pair in confine state of sp^2 carbon clusters combined with sp^3 matrix and rGO luminescence was caused by disappearance of oxygen-related functional groups that facilitate percolation of paths among sp^2 clusters. In case of BN nanosheets, PL spectra appeared at 460 nm which was ascribed to electronic transition including individual or mutual transition among 2p states of BN bands. In XPS spectra of GO, O 1 s peak positioned at 530.6 eV originated from C=O and O=C–OH groups and C 1 s significant peak with binding energy of ~ 284.0 eV was caused by graphitic C–C peak owing to

sp^2 carbon bond and oxygen-containing functional groups. In spectra obtained from MoS_2, S 2p region that exhibited single doublet peaks of $2p_{3/2}$ (161.7 eV) and $2p_{1/2}$ (162.8 eV) confirmed the presence of Mo–S bond. Endothermic peak of GO is evidenced at 213 °C which elucidated to GO thermolysis. In TGA curve, initially GO lost mass of about 20% below 100 °C owing to water evaporation and pyrolysis of oxygen-containing –OH, COOH groups. In case of MoS_2, oxidation occurred between 320 and 650 °C with weight loss of 25%, which revealed thermal decomposition. Strong photocatalytic activity was exhibited by rGO and MoS_2 which degraded 60% and 55% of MB concentration, respectively. The experimental results indicate that the products synthesized in this study can be regarded as excellent nanocatalysts suitable for elimination of organic pollutants from wastewater. It was also shown that the techniques and materials employed here for the synthesis of nanocatalysts exhibit no hazardous behavior in wastewater treatment process.

Acknowledgements The authors are grateful to the financial support by the higher education commission Pakistan through start research grant project # 21-1669/SRGP/R&D/HEC/2017 and CAS-TWAS President's Fellowship for international PhD students China. Support provided by the Research Institute, King Fahd University of Petroleum & Minerals, Dhahran, is also appreciated.

Compliance with ethical standards

Conflict of interest There are no conflicts of interest to declare.

References

Ahmed ASA, Xiang W, Hu X, Qi C, Amiinu IS, Zhao X (2018) Si3N4/MoS_2-PEDOT: pSS composite counter electrode for bifacial dye-sensitized solar cells. Sol Energy 173:1135–1143

Alam SN, Sharma N, Kumar L (2017) Synthesis of graphene oxide (GO) by modified hummers method and its thermal reduction to obtain reduced graphene oxide (rGO). Graphene 06(01):1–18

Alhassan SM, Qutubuddin S, Schiraldi DA, Agag T, Ishida H (2013) Preparation and thermal properties of graphene oxide/main chain benzoxazine polymer. Eur Polym J 49(12):3825–3833

Ali A et al (2019) Ultrathin MoS_2 nanosheets for high-performance photoelectrochemical applications via plasmonic coupling with Au nanocrystals. Nanoscale 11(16):7813–7824

Altaf S et al (2020) Synthesis and characterization of binary selenides of transition metals to investigate its photocatalytic, antimicrobial and anticancer efficacy. Appl Nanosci. https://doi.org/10.1007/s13204-020-01350-w

Aqeel M et al (2019) TiO_2 @ RGO (reduced graphene oxide) doped nanoparticles demonstrated improved photocatalytic activity. Mater Res Express 6(8):086215

Arshad A et al (2017) Solar light triggered catalytic performance of graphene-CuO nanocomposite for waste water treatment. Ceram Int 43(14):10654–10660

Bano N, Hussain I, El-Naggar AM, Albassam AA (2019) Reduced graphene oxide nanocomposites for optoelectronics applications. Appl Phys A 125(3):215

Beshkova M, Yakimova RJV (2020) Properties and potential applications of two-dimensional AlN. Vacuum 176:109231

Bozheyev F, Valiev D, Nemkayeva R (2017) Pulsed cathodoluminescence and Raman spectra of MoS_2 nanocrystals at different excitation electron energy densities and laser wavelengths. J Lumin 188:529–532

Cai Q et al (2017) Raman signature and phonon dispersion of atomically thin boron nitride. Nanoscale 9(9):3059–3067

Cai X, Luo Y, Liu B, Cheng HM (2018) Preparation of 2D material dispersions and their applications. Chem Soc Rev 47(16):6224–6266

Cassabois G, Valvin P, Gil B (2016) Hexagonal boron nitride is an indirect bandgap semiconductor. Nat Photonics 10(4):262–266

Chacko L, Rastogi PK, Aneesh PM (2019) Phase engineering from 2H to 1T-MoS_2 for efficient ammonia PL sensor and electrocatalyst for hydrogen evolution reaction. J Electrochem Soc 166(8):H263–H271

Chenet D (2016) 2D materials: synthesis, characterization, and applications. Columbia University, New York

Church RB, Hu K, Magnacca G, Cerruti M (2016) Intercalated species in multilayer graphene oxide: insights gained from in situ FTIR spectroscopy with probe molecule delivery. J Phys Chem C 120(40):23207–23211

Cui J et al (2019) Ultrahigh recovery of fracture strength on mismatched fractured amorphous surfaces of silicon carbide. ACS Nano 13(7):7483–7492

Dadvar E, Kalantary RR, Ahmad Panahi H, Peyravi M (2017) Efficiency of polymeric membrane graphene oxide-TiO_2 for removal of azo dye. J Chem 2017:1–13

Demas NG, Timofeeva EV, Routbort JL, Fenske GR (2012) Tribological effects of BN and MoS_2 nanoparticles added to polyalphaolefin oil in piston skirt/cylinder liner tests. Tribol Lett 47(1):91–102

Deng F et al (2016) Fabrication of hierarchically porous reduced graphene oxide/SnIn4S8 composites by a low-temperature coprecipitation strategy and their excellent visible-light photocatalytic mineralization performance. Catalysts 6(8):113

Ding Y, Torres-Davila F, Khater A, Nash D, Blair R, Tetard L (2018a) Defect engineering in boron nitride for catalysis. MRS Commun 8(03):1236–1243

Ding JJ, Chen HX, Feng DQ, Fu HW (2018b) Investigation on photoluminescence emission of (reduced) graphene oxide paper. In: IOP conference series: materials science and engineering, vol 292, p 012097

Doll GL, Speck JS, Dresselhaus G, Dresselhaus MS, Nakamura K, Tanuma SI (1989) Intercalation of hexagonal boron nitride with potassium. J Appl Phys 66(6):2554–2558

Eda G, Yamaguchi H, Voiry D, Fujita T, Chen M, Chhowalla M (2011) Photoluminescence from chemically exfoliated MoS_2. Nano Lett 11(12):5111–5116

Eginligil M et al (2015) Dichroic spin-valley photocurrent in monolayer molybdenum disulphide. Nat Commun 6:7636

Eigler S, Dotzer C, Hirsch A, Enzelberger M, Müller P (2012) Formation and decomposition of CO_2 intercalated graphene oxide. Chem Mater 24(7):1276–1282

Fan D et al (2016a) Hexagonal boron nitride nanosheets exfoliated by sodium hypochlorite ball mill and their potential application in catalysis. Ceram Int 42(6):7155–7163

Fan B et al (2016b) Facile one-pot preparation of silver/reduced graphene oxide nanocomposite for cancer photodynamic and photothermal therapy. J Nanosci Nanotechnol 16(7):7049–7054

Feng SH, Li GH (2017) Hydrothermal and solvothermal syntheses. In: Modern inorganic synthetic chemistry. https://doi.org/10.1016/B978-0-444-53599-3.10004-6

Feng PX, Sajjad M (2012) Few-atomic-layer boron nitride sheets syntheses and applications for semiconductor diodes. Mater Lett 89:206–208

Fosso-Kankeu E, Spiro MJ, Waanders F, Kumar N, Ray SS, Lemmer N (2018) Hydrothermal synthesis, characterisation and adsorption testing of MoS_2-zeolite for the removal of lead in an aqueous solution. In: Presented at the ASETH-18,ACABES-18 & EBHSSS-18 Nov. 19–20 2018 Cape Town (South Africa)

Frank O et al (2011) Raman 2D-band splitting in graphene: theory and experiment. ACS Nano 5(3):2231–2239

Gayathri S, Jayabal P, Kottaisamy M, Ramakrishnan V (2014) Synthesis of few layer graphene by direct exfoliation of graphite and a Raman spectroscopic study. AIP Adv 4(2):027116

Geick R, Perry CH, Rupprecht G (1966) Normal modes in hexagonal boron nitride. Phys Rev 146(2):543–547

Geng X, Yi J (2019) The development of high-temperature superconductors and 2D iron-based superconductors. In: Nano-sized multifunctional materials, pp 117–144. https://doi.org/10.1016/B978-0-12-813934-9.00006-2

Gnanaprakasam A, Sivakumar VM, Thirumarimurugan M (2015) Influencing parameters in the photocatalytic degradation of organic effluent via nanometal oxide catalyst: a review. Indian J Mater Sci 2015:1–16

Gołasa K et al (2014) Multiphonon resonant Raman scattering in MoS_2. Appl Phys Lett 104(9):092106

Golmakani MH, Khaki V, Babakhani A (2018) Formation mechanism of Fe-Mo master alloy by aluminothermic reduction of MoS_2-Fe_2O^3 in the presence of lime. J Min Metall Sect B 54(2):233–241

Gong Y, Li D, Fu Q, Pan C (2015) Influence of graphene microstructures on electrochemical performance for supercapacitors. Prog Nat Sci Mater Int 25(5):379–385

Grossman KD, Sakthivel TS, Dillier C, Petersen EL, Seal S (2016) Effect of amine-modified boron nitride (BN) on ammonium perchlorate decomposition. RSC Adv 6(92):89635–89641

Gurunathan S, Han JW, Eppakayala V, Kim JH (2013) Microbial reduction of graphene oxide by Escherichia coli: a green chemistry approach. Colloids Surf B Biointerfaces 102:772–777

Gurunathan S et al (2015) Reduced graphene oxide-silver nanoparticle nanocomposite: a potential anticancer nanotherapy. Int J Nanomed 10:6257–6276

Haldorai Y, Kim B-K, Jo Y-L, Shim J-JJMC (2014) Ag@ graphene oxide nanocomposite as an efficient visible-light plasmonic photocatalyst for the degradation of organic pollutants: a facile green synthetic approach. Mater Chem Phys 143(3):1452–1461

Hasan J et al (2020) Application of chemically exfoliated boron nitride nanosheets doped with Co to remove organic pollutants rapidly from textile water. Nanoscale Res Lett 15(1):75. https://doi.org/10.1186/s11671-020-03315-y

Hassan J, Ikram M, Ul-Hamid A, Imran M, Aqeel M, Ali S (2020) Application of chemically exfoliated boron nitride nanosheets doped with Co to remove organic pollutants rapidly from textile water. Nanoscale Res Lett 15(1):75

Ikram M et al (2020a) Bimetallic Ag/Cu incorporated into chemically exfoliated MoS_2 nanosheets to enhance its antibacterial potential: in silico molecular docking studies. Nanotechnology 31(27):275704

Ikram M, Raza A, Imran M, Ul-Hamid A, Shahbaz A, Ali S (2020b) Hydrothermal synthesis of silver decorated reduced graphene oxide (rGO) nanoflakes with effective photocatalytic activity for wastewater treatment. Nanoscale Res Lett 15(1):95

Ikram M et al (2020c) Reduced graphene oxide nanosheets doped by Cu with highly efficient visible light photocatalytic behavior. J Alloys Compd 837:155588

Ikram M et al (2020d) Promising performance of chemically exfoliated Zr-doped MoS2 nanosheets for catalytic and antibacterial applications. RSC Adv 10(35):20559–20571

Ikram M et al (2020e) 2D chemically exfoliated hexagonal boron nitride (hBN) nanosheets doped with Ni: synthesis, properties and catalytic application for the treatment of industrial wastewater. Appl Nanosci. https://doi.org/10.1007/s13204-020-01439-2

Ikram M et al (2020f) Bactericidal behavior of chemically exfoliated boron nitride nanosheets doped with zirconium. Appl Nanosci. https://doi.org/10.1007/s13204-020-01412-z

Ikram M et al (2020g) Evaluation of antibacterial and catalytic potential of copper-doped chemically exfoliated boron nitride nanosheets. Ceram Int. https://doi.org/10.1016/j.ceramint.2020.05.180

Jayanti DN, Nugraheni AY, Baqiya MA (2017) Photoluminescence of reduced graphene oxide prepared from old coconut shell with carbonization process at varying temperatures. In: IOP conference series: materials science and engineering, vol 196

Ji C, Levitas VI, Zhu H, Chaudhuri J, Marathe A, Ma Y (2012) Shear-induced phase transition of nanocrystalline hexagonal boron nitride to wurtzitic structure at room temperature and lower pressure. Proc Natl Acad Sci USA 109(47):19108–19112

Jiang T, Kuila T, Kim NH, Ku B-C, Lee JH (2013) Enhanced mechanical properties of silanized silica nanoparticle attached graphene oxide/epoxy composites. Compos Sci Technol 79:115–125

Junaid M et al (2019) The study of Fe-doped CdS nanoparticle-assisted photocatalytic degradation of organic dye in wastewater. Appl Nanosci 9(8):1593–1602

Kaniyoor A, Ramaprabhu S (2012) A Raman spectroscopic investigation of graphite oxide derived graphene. AIP Adv 2(3):032183

Ke J et al (2017) Facile assembly of Bi_2O_3/Bi_2S_3/MoS_2 n-p heterojunction with layered n-Bi_2O_3 and p-MoS_2 for enhanced photocatalytic water oxidation and pollutant degradation. Appl Catal B 200:47–55

Khanra P, Kuila T, Kim NH, Bae SH, Yu D-S, Lee JH (2012) Simultaneous bio-functionalization and reduction of graphene oxide by baker's yeast. Chem Eng J 183:526–533

Khurshid F, Jeyavelan M, Hudson MSL, Nagarajan S (2019) Ag-doped ZnO nanorods embedded reduced graphene oxide nanocomposite for photo-electrochemical applications. R Soc Open Sci 6(2):181764

Krishnamoorthy K, Veerapandian M, Yun K, Kim SJ (2013) The chemical and structural analysis of graphene oxide with different degrees of oxidation. Carbon 53:38–49

Kumar V, Nikhil K, Roy P, Lahiri D, Lahiri I (2016) Emergence of fluorescence in boron nitride nanoflakes and its application in bioimaging. RSC Adv 6(53):48025–48032

Kumar S, Sharma V, Bhattacharyya K, Krishnan V (2017) N-doped ZnO–MoS_2 binary heterojunctions: the dual role of 2D MoS_2 in the enhancement of photostability and photocatalytic activity under visible light irradiation for tetracycline degradation. Mater Chem Front 1(6):1093–1106

Kumar A, Sadanandhan AM, Jain SL (2019) Silver doped reduced graphene oxide as a promising plasmonic photocatalyst for oxidative coupling of benzylamines under visible light irradiation. New J Chem 43(23):9116–9122

Kumbhakar P et al (2015) Nonlinear optical properties and temperature-dependent UV–Vis absorption and photoluminescence emission in 2D hexagonal boron nitride nanosheets. Adv Opt Mater 3(6):828–835

Le GTT, Manyam J, Opaprakasit P, Chanlek N, Grisdanurak N, Sreearunothai P (2018) Divergent mechanisms for thermal

reduction of graphene oxide and their highly different ion affinities. Diam Relat Mater 89:246–256
Lee D, Song SH (2017) Ultra-thin ultraviolet cathodoluminescent device based on exfoliated hexagonal boron nitride. RSC Adv 7(13):7831–7835
Lewandowska R (2014) Number of layers of MoS_2 determined using Raman Spectroscopy
Li X, Zhu H (2015) Two-dimensional MoS_2: properties, preparation, and applications. J Materiomics 1(1):33–44
Li J et al (2013) Activated boron nitride as an effective adsorbent for metal ions and organic pollutants. Sci Rep 3:3208
Li LH, Cervenka J, Watanabe K, Taniguchi T, Chen YJAN (2014) Strong oxidation resistance of atomically thin boron nitride nanosheets. ACS Nano 8(2):1457–1462
Li X, Shan J, Zhang W, Su S, Yuwen L, Wang LJS (2017) Recent advances in synthesis and biomedical applications of two-dimensional transition metal dichalcogenide nanosheets. Small 13(5):1602660
Li X, Wu L, Hao L, Fu Y (2018) Emerging 2D nanomaterials for supercapacitor applications. In: Emerging materials for energy conversion and storage. https://doi.org/10.1016/B978-0-12-813794-9.00005-3
Li M, Cui Z, Li E (2019) Silver-modified MoS_2 nanosheets as a high-efficiency visible-light photocatalyst for water splitting. Ceram Int 45(11):14449–14456
Liu L, Li Y (2014) Understanding the reaction mechanism of photocatalytic reduction of CO_2 with H_2O on TiO_2-based photocatalysts: a review. Aerosol Air Qual Res 14(2):453–469
Liu H, Chen X, Deng L, Su X, Guo K, Zhu Z (2016) Preparation of ultrathin 2D MoS_2/graphene heterostructure assembled foam-like structure with enhanced electrochemical performance for lithium-ion batteries. Electrochim Acta 206:184–191
Liu J, Ma Q, Huang Z, Liu G, Zhang H (2019a) Recent progress in graphene-based noble-metal nanocomposites for electrocatalytic applications. Adv Mater 31(9):e1800696
Liu Q, Hu C, Wang X (2019b) One-pot solvothermal synthesis of water-soluble boron nitride nanosheets and fluorescent boron nitride quantum dots. Mater Lett 234:306–310
Lu S, Li S, Yu J, Yuan Z, Qi B (2013) Epoxy nanocomposites filled with thermotropic liquid crystalline epoxy grafted graphene oxide. RSC Adv 3(23):8915–8923
Luceño-Sánchez JA, Maties G, Gonzalez-Arellano C, Díez-Pascual AM (2018) Synthesis and characterization of graphene oxide derivatives via functionalization reaction with hexamethylene diisocyanate. Nanomaterials 8(11):870. https://doi.org/10.3390/nano8110870
Ma L, Xu L, Xu X, Zhou X, Luo J, Zhang L (2016) Cobalt-doped edge-rich MoS_2/nitrogenated graphene composite as an electrocatalyst for hydrogen evolution reaction. Mater Sci Eng B 212:30–38
Mahdizadeh A, Farhadi S, Zabardasti A (2017) Microwave-assisted rapid synthesis of graphene-analogue hexagonal boron nitride (h-BN) nanosheets and their application for the ultrafast and selective adsorption of cationic dyes from aqueous solutions. RSC Adv 7(85):53984–53995
Mangalam J, Kumar M, Sharma M, Joshi M (2019) High adsorptivity and visible light assisted photocatalytic activity of silver/reduced graphene oxide (Ag/rGO) nanocomposite for wastewater treatment. Nano-Struct Nano-Objects 17:58–66
Manzeli S, Ovchinnikov D, Pasquier D, Yazyev OV, Kis A (2017) 2D transition metal dichalcogenides. Nat Rev Mater 2(8):17033
Mishra AK, Lakshmi KV, Huang L (2015) Eco-friendly synthesis of metal dichalcogenides nanosheets and their environmental remediation potential driven by visible light. Sci Rep 5:15718
Morgan H, Rout CS, Late DJ (2019) Introduction. Fundamentals and sensing applications of 2D materials. Woodhead Publishing, Duxford, pp 1–3
Mouri S, Miyauchi Y, Matsuda KJNL (2013) Tunable photoluminescence of monolayer MoS_2 via chemical doping. Nano Lett 13(12):5944–5948
Nafees M, Ikram M, Ali SJDJNB (2015) Thermal behavior and decomposition of copper sulfide nanomaterial synthesized by aqueous sol method. Dig J Nanomater Biostruct 10(2):635–641
Ng LW, Hu G, Howe RC, Zhu X, Yang Z, Jones CG, Hasan T (2019) 2D material production methods. In: Printing of graphene and related 2D materials. Springer, Cham. https://doi.org/10.1007/978-3-319-91572-2_3
Ngidi NPD, Ollengo MA, Nyamori VO (2019) Effect of doping temperatures and nitrogen precursors on the physicochemical, optical, and electrical conductivity properties of nitrogen-doped reduced graphene oxide. Materials (Basel) 12(20):3376
Ohtani B (2010) Photocatalysis A to Z—what we know and what we do not know in a scientific sense. J Photochem Photobiol C 11(4):157–178
Pal SK (2015) Versatile photoluminescence from graphene and its derivatives. Carbon 88:86–112
Patil S, Harle A, Sathaye S, Patil K (2014) Development of a novel method to grow mono-/few-layered MoS_2 films and MoS_2–graphene hybrid films for supercapacitor applications. CrystEngComm 16(47):10845–10855
Phung HNT, Truong ND, Duong PA, Tuan Hung LV (2018) Influence of MoS2 deposition time on the photocatalytic activity of MoS_2/V, N co-doped TiO_2 heterostructure thin film in the visible light region. Current Applied Physics 18(6):737–743
Pineda-León H et al (2018) Synthesis and characterization of molibdenum sulfide nanoparticles by a new chemical reaction formulation. Chalcogenide Lett 15(8):419–424
Placidi M et al (2015) Multiwavelength excitation Raman scattering analysis of bulk and two-dimensional MoS_2: vibrational properties of atomically thin MoS_2 layers. 2D Mater 2(3):035006
Qumar U et al (2020) Synergistic effect of Bi-doped exfoliated MoS_2 nanosheets on their bactericidal and dye degradation potential. Dalton Trans 49(16):5362–5377
Rafiq A et al (2019) Photocatalytic and catalytic degradation of organic dye by uncapped and capped ZnS quantum dots. Mater Res Express 6(5):055801
Rashid M et al (2020) Photocatalytic, dye degradation, and bactericidal behavior of Cu-doped ZnO nanorods and its molecular docking analysis. Dalton Trans. https://doi.org/10.1039/D0DT01397H
Raza A et al (2019) Enhanced industrial dye degradation using Co doped in chemically exfoliated MoS_2 nanosheets. Appl Nanosci 10(5):1535–1544
Ren PG, Yan DX, Ji X, Chen T, Li ZM (2011) Temperature dependence of graphene oxide reduced by hydrazine hydrate. Nanotechnology 22(5):055705
Sattar U, Ikram M, Junaid M, Aqeel M, Imran M, Ali S (2019) Annealing effect on synthesized ZnS/TiO_2 nanocomposite for treatment of industrial wastewater. Mater Res Express 6(11):115050
Sengupta I, Chakraborty S, Talukdar M, Pal SK, Chakraborty S (2018) Thermal reduction of graphene oxide: how temperature influences purity. J Mater Res 33(23):4113–4122
Sheng Y et al (2019) Sol-gel synthesized hexagonal boron nitride/titania nanocomposites with enhanced photocatalytic activity. Appl Surf Sci 465:154–163
Silly MG et al (2007) Luminescence properties of hexagonal boron nitride: cathodoluminescence and photoluminescence spectroscopy measurements. Phys Rev B 75(8):085205
Singh B et al (2016) Nanostructured boron nitride with high water dispersibility for boron neutron capture therapy. Sci Rep 6:35535
Some S et al (2013) High-quality reduced graphene oxide by a dual-function chemical reduction and healing process. Sci Rep 3:1929

Song J, Wang X, Chang C-T (2014) Preparation and characterization of graphene oxide. J Nanomater 2014:1–6

Štengl V, Henych J, Kormunda M (2014) Self-assembled BN and BCN quantum dots obtained from high intensity ultrasound exfoliated nanosheets. Sci Adv Mater 6(6):1106–1116

Sun L (2016) Optical characterization of molybdenum disulfide by raman and photoluminescence. https://doi.org/10.32657/10356/66936

Suram SK, Newhouse PF, Gregoire JM (2016) High throughput light absorber discovery, part 1: an algorithm for automated Tauc analysis. ACS Comb Sci 18(11):673–681

Suresh R et al (2018) Effect of reduced graphene oxide on the structural, optical, adsorption and photocatalytic properties of iron oxide nanoparticles. New J Chem 42(11):8485–8493

Tang CY, Zulhairun AK, Wong TW, Alireza S, Marzuki MSA, Ismail AF (2019) Water transport properties of boron nitride nanosheets mixed matrix membranes for humic acid removal. Heliyon 5(1):e01142

Thangappan R et al (2016) Graphene decorated with MoS_2 nanosheets: a synergetic energy storage composite electrode for supercapacitor applications. Dalton Trans 45(6):2637–2646

Thangasamy P, Sathish M (2015) Supercritical fluid processing: a rapid, one-pot exfoliation process for the production of surfactant-free hexagonal boron nitride nanosheets. CrystEngComm 17(31):5895–5899

Tian N et al (2016) Utilization of MoS2 nanosheets to enhance the photocatalytic activity of ZnO for the aerobic oxidation of benzyl halides under visible light. Ind Eng Chem Res 55(32):8726–8732

Tiwari SK, Hatui G, Oraon R, De Adhikari A, Nayak GC (2017) Mixing sequence driven controlled dispersion of graphene oxide in PC/PMMA blend nanocomposite and its effect on thermo-mechanical properties. Curr Appl Phys 17(9):1158–1168

Traina M, Pegoretti A (2012) In situ reduction of graphene oxide dispersed in a polymer matrix. J Nanopart Res 14(4):801

Tun S, Naing K (2020) Preparation and characterization of magnesium aluminate nanoparticles by hydrothermal method. In: Dagon University Commemoration of 25th Anniversary Silver Jubilee Research Journal 2019, vol 9, No. 2

Vargas-Bernal R (2016) Graphene against other two-dimensional materials: a comparative study on the basis of electronic applications. In: Two-dimensional materials—synthesis, characterization and potential applications. https://doi.org/10.5772/63916

Vattikuti SVP, Byon C (2015) Synthesis and characterization of molybdenum disulfide nanoflowers and nanosheets: nanotribology. J Nanomater 2015:1–11

Vattikuti SVP, Byon C, Reddy CV, Ravikumar RVSSN (2015) Improved photocatalytic activity of MoS_2 nanosheets decorated with SnO_2 nanoparticles. RSC Adv 5(105):86675–86684

Veeramalai CP, Li F, Liu Y, Xu Z, Guo T, Kim TW (2016) Enhanced field emission properties of molybdenum disulphide few layer nanosheets synthesized by hydrothermal method. Appl Surf Sci 389:1017–1022

Viezbicke BD, Patel S, Davis BE, Birnie DP (2015) Evaluation of the Tauc method for optical absorption edge determination: ZnO thin films as a model system. Phys Status Solidi (b) 252(8):1700–1710

Vu MC et al (2018) Self-assembly of carbon nanotubes and boron nitride via electrostatic interaction for epoxy composites of high thermal conductivity and electrical resistivity. Macromol Res 26(6):521–528

Wang Q, Li J (2007) Facilitated lithium storage in MoS_2 overlayers supported on coaxial carbon nanotubes. J Phys Chem 111(4):1675–1682

Wang J et al (2012a) Direct synthesis of hydrophobic graphene-based nanosheets via chemical modification of exfoliated graphene oxide. J Nanosci Nanotechnol 12(8):6460–6466

Wang X et al (2012b) Large-surface-area BN nanosheets and their utilization in polymeric composites with improved thermal and dielectric propertie. Nanoscale Res Lett 7(1):662

Wang J, Li G, Li L (2016a) Synthesis strategies about 2D materials. In: Two-dimensional materials—synthesis, characterization and potential applications

Wang J et al (2016b) Enhanced exfoliation effect of solid auxiliary agent on the synthesis of biofunctionalized MoS_2 using grindstone chemistry. Part Part Syst Charact 33(11):825–832

Wang Z, Cheng Y, Shao Y, Xie Q, Wu G (2016c) Thermal conductivity and electric breakdown strength properties of epoxy/alumina/boron nitride nanosheets composites. In: 2016 IEEE international conference on dielectrics (ICD), vol 1. IEEE, pp 355–358

Wang B et al (2018a) New deformation-induced nanostructure in silicon. Nano Lett 18(7):4611–4617

Wang T et al (2018b) Tulip-like MoS_2 with a single sheet tapered structure anchored on N-doped graphene substrates via C–O–Mo bonds for superior sodium storage. J Mater Chem 6(47):24433–24440

Watanabe K, Taniguchi T (2009) Jahn–Teller effect on exciton states in hexagonal boron nitride single crystal. Phys Rev B 79(19):193104

Weng Q, Wang X, Zhi C, Bando Y, Golberg DJAN (2013) Boron nitride porous microbelts for hydrogen storage. ACS Nano 7(2):1558–1565

Windom BC, Sawyer WG, Hahn DW (2011) A Raman spectroscopic study of MoS_2 and MoO_3: applications to tribological systems. Tribol Lett 42(3):301–310

Wu Z, Wang D, Wang Y, Sun A (2010) Preparation and tribological properties of MoS_2 nanosheets. Adv Eng Mater 12(6):534–538

Wu W, Lv X, Wang J, Xie J (2017) Integrating AgI/AgBr biphasic heterostructures encased by few layer h-BN with enhanced catalytic activity and stability. J Colloid Interface Sci 496:434–445

Yang D et al (2009) Chemical analysis of graphene oxide films after heat and chemical treatments by X-ray photoelectron and Micro-Raman spectroscopy. Carbon 47(1):145–152

Yaragalla S, Rajendran R, Jose J, AlMaadeed MA, Kalarikkal N, Thomas S (2016) Preparation and characterization of green graphene using grape seed extract for bioapplications. Mater Sci Eng C Mater Biol Appl 65:345–353

Yasin G et al (2018) Exploring the nickel–graphene nanocomposite coatings for superior corrosion resistance: manipulating the effect of deposition current density on its morphology, mechanical properties, and erosion-corrosion performance. Adv Eng Mater 20(7):1701166

Yein WT, Wang Q, Li Y, Wu X (2019) Piezoelectric potential induced the improved micro-pollutant dye degradation of Co doped MoS_2 ultrathin nanosheets in dark. Catal Commun 125:61–65

Yi M, Zhang C (2018) The synthesis of two-dimensional MoS_2 nanosheets with enhanced tribological properties as oil additives. RSC Adv 8(17):9564–9573

Yuan S et al (2016) Pure & crystallized 2D boron nitride sheets synthesized via a novel process coupling both PDCs and SPS methods. Sci Rep 6:20388

Zhang Z, Song Y, Xu C, Guo DJSM (2012) A novel model for undeformed nanometer chips of soft-brittle HgCdTe films induced by ultrafine diamond grits. Scr Mater 67(2):197–200

Zhang Z et al (2017a) A novel approach of mechanical chemical grinding. J Alloys Compd 726:514–524

Zhang K, Feng Y, Wang F, Yang Z, Wang J (2017b) Two dimensional hexagonal boron nitride (2D-hBN): synthesis, properties and applications. J Mater Chem C 5(46):11992–12022

Zhang B et al (2017c) High-efficient liquid exfoliation of boron nitride nanosheets using aqueous solution of alkanolamine. Nanoscale Res Lett 12(1):596

Zhang Z, Shi Z, Du Y, Yu Z, Guo L, Guo DJASS (2018) A novel approach of chemical mechanical polishing for a titanium alloy using an environment-friendly slurry. Appl Surf Sci 427:409–415

Zhang Z, Cui J, Zhang J, Liu D, Yu Z, Guo DJASS (2019) Environment friendly chemical mechanical polishing of copper. Appl Surf Sci 467:5–11

Zhang Z et al (2020a) Macroscale superlubricity enabled by graphene-coated surfaces. Adv Sci (Weinh) 7(4):1903239

Zhang Z, Liao L, Wang X, Xie W, Guo DJASS (2020b) Development of a novel chemical mechanical polishing slurry and its polishing mechanisms on a nickel alloy. Appl Surf Sci 506:144670

Zhong B, Zhang X, Xia L, Yu Y, Wen G (2017) Large-scale fabrication and utilization of novel hexagonal/turbostratic composite boron nitride nanosheets. Mater Des 120:266–272